Manuscript number JQSR_2018_714_R2

Frequency and dynamics of millennial-scale variability during Marine Isotope Stage 19: Insights from the Sulmona Basin (central Italy)

E. Regattieri[1,2]; B. Giaccio[3]; G. Mannella[1]; G. Zanchetta[1]; S. Nomade[4]; A. Tognarelli[1], N. Perchiazzi[1]; H. Vogel[5]; C. Boschi[2]; R.N. Drysdale[6,7]; B. Wagner[8]; M. Gemelli[1]; P.C. Tzedakis[9]

[1]Dipartimento di Scienze della Terra, University of Pisa, Via S. Maria 53, 56126 Pisa, Italy

[2]Istituto di Geoscienze e Georisorse, IGG-CNR, Via Moruzzi 1, 56126 Pisa, Italy

[3]Istituto di Geologia Ambientale e Geoingegneria, IGAG-CNR, Via Salaria km. 29.4 Monterotondo Rome, Italy

[4]Laboratoire des Sciences du Climat et de l'Environnement, IPSL, UMR8212, laboratoire CEA/CNRS/UVSQ et Université de Paris-Saclay, Gif-Sur-Yvette, France

[5]Institute of Geological Sciences & Oeschger Centre for Climate Change Research, University of Bern, Switzerland

[6]School of Geography, University of Melbourne, Victoria 3010, Australia

[7]EDYTEM, UMR CNRS 5204, Université de Savoie-Mont Blanc, 73376 Le Bourget du Lac cedex, France

[8]Institute of Geology and Mineralogy, University of Cologne, Zülpicher Str. 49a, 50674 Köln, Germany.

[9]Environmental Change Research Centre, Department of Geography, University College London, England.

Abstract

Among past interglacial periods, Marine Isotope Stage (MIS) 19 is particularly interesting because its orbital geometry is very similar to that of the present interglacial. Here we present a high-resolution (sub-centennial) multiproxy record covering the ca. 790-770 ka interval, i.e. the interglacial MIS 19c and the ensuing glacial inception of MIS 19b, from a lacustrine sediment sequence retrieved from the Sulmona Basin (central Italy). The record has an independent chronology based on radiometric dating of six volcanic ash layers, and the resulting age model has a mean associated uncertainty of ± 2.6 kyr. Variations in sediment geochemistry and mineralogy are interpreted in terms of past hydrological and

temperature changes. Several millennial and sub-millennial events of reduced precipitation are well expressed. Comparisons with continental and marine records from the mid-latitude and sub-polar North Atlantic suggest a broad spatial expression for the observed events. Events occurring within the interglacial are not clearly associated with changes in marine proxies in the Iberian Margin, although similarities with the record from the sub-polar North Atlantic can be recognized and tentatively linked to changes in local hydrography having a downstream effect amplified by changes in atmospheric circulation. During the glacial inception, however, changes in the Sulmona record are coherent with changes in North Atlantic records, with drier events likely associated with meltwater-induced intervals of AMOC weakening. An event at ca. 785.6 ka may also reflect oceanic changes caused by freshwater discharges from residual ice-sheets and an outburst flood, similar to the 8.2 ka event in the Holocene.

Keywords: Stable isotope geochemistry, interglacial variability, central Italy, lacustrine succession, MIS 19

1. Introduction

The recovery of high-resolution records of climate variability from oceans, ice-sheets and continental archives has profoundly modified our perspective on global climate change by revealing the pervasive existence of very rapid and high-amplitude climate changes in the past (e.g. Gottschalk et al., 2015). Although such abrupt climatic changes can be triggered by different forcing, it is conceivable that human activity has likely increased their probability (Alley et al., 2003). Thus, the recognition of short-term (i.e. multi-decadal to sub-millennial), global-scale, climate variability during previous interglacial periods is of fundamental importance to provide the context of natural variability in which human-induced changes operate (Tzedakis et al., 2009).

Among older interglacial periods, Marine Isotope Stage (MIS) 19c has received particular attention due to its orbital geometry, which was very similar to that of the present interglacial (i.e., low eccentricity

and weak precession, and similar phasing between precession and obliquity: Berger and Loutre, 1991; Pol et al., 2010; Tzedakis, 2010; Tzedakis et al., 2012). Modelling studies have highlighted that this period is the best analogue for the Holocene when annual and seasonal temperatures are taken into account, although it appears less similar when the summer-half yearly insolation is considered (Yin and Berger 2010, 2012). Because MIS 19c occurred before the Mid-Brunhes Event (~450 ka) – i.e. before the culmination of a series of changes of the global climate system resulting in the establishment of longer and deeper glacial-interglacial cycles (e.g. Head et al., 2008) – it was also characterized by slightly lower global temperatures and atmospheric CO_2 concentrations with respect to the preindustrial Holocene, and possibly by higher residual global ice-volume (Bintanja et al. 2005; Bintanja and van de Wal 2008; Lüthi et al., 2008; Lisiecki and Raymo, 2005; Elderfield et al., 2012). Millennial- to centennial-scale climate oscillations during MIS 19, and particularly within substage MIS 19c, have been previously reported from both marine and continental archives (Sánchez-Goñi et al., 2016; Maegakiuchi et al., 2017; Oliveira et al., 2018; Kleiven et al., 2011; Maiorano et al., 2016; Marino et al., 2015; Ferretti et al., 2015; Nomade et al., 2019). The findings of a ~5-kyr periodicity, i.e., similar to the fourth harmonic of precession, in both the coupled marine-pollen record from the southern Iberian margin (site U1385, Sánchez-Goñi et al., 2016) and in the planktonic and benthic $\delta^{18}O$ record from low to mid-latitude North Atlantic and Mediterranean records (Ferretti et al., 2015; Weirauch et al., 2008; Nomade et al., 2019) led to the suggestion that variations in the tropical seasonal insolation cycle, driven by precession and its harmonics, caused periodic oscillations in the latitudinal thermal gradient. These oscillations were considered capable of altering both sea-surface conditions and westerly wind trajectories, modifying the northward transport of heat and water vapour (Sánchez-Goñi et al., 2016). Further north, however, the record of outflow speed from the Nordic Sea and the isotopic composition of surface and bottom waters from site ODP-983 (Fig. 1, Kleiven et al., 2003, 2011), located near the eastern source of North Atlantic Deep Water (NADW), shows a series of millennial-scale episodes of reduced ventilation of intermediate

72 waters and reduction in deep convection strength during the whole MIS 19 period. These oscillations
73 have been related to changes in local convection and to reduced NADW formation, leading to intervals
74 of weakened Atlantic Meridional Overturning Circulation (AMOC) (Kleiven et al., 2011). As AMOC
75 disruptions affect also Mediterranean climate, causing decreases in temperature and precipitation (e.g.
76 Columbu et al., 2017; Drysdale et al., 2007; Fletcher et al., 2013; Margari et al., 2009; Regattieri et al.,
77 2015, 2016, 2018; Tzedakis et al., 2018), the ODP-983 record points to high-latitude forcing of the
78 observed variability. These contrasting findings thus leave open questions about oceanic and atmospheric
79 mechanisms operating at sub-millennial scales during MIS 19 and, particularly, in its interglacial portion,
80 and it is not clear if and how these processes can be linked to boundary conditions. Part of this uncertainty
81 is also due to the lack of robust and independent chronologies, an issue which until now has clearly
82 hampered our capability to asses the timing, rate, propagation and duration of changes.

83 Here we present a multiproxy biogeochemical record (high resolution stable oxygen and carbon isotope
84 on lacustrine calcite, low-resolution elemental and mineralogical composition on the bulk sediment,
85 biogenic silica content) from a stratigraphic interval containing the MIS 19c, which is part of the
86 lacustrine succession hosted in the Sulmona Basin (central Italy, Fig. 1). Sediment proxies from Sulmona
87 Basin record local environmental conditions, which can be linked to North Atlantic climate variability
88 (Giaccio et al., 2015; Regattieri et al., 2015, 2016, 2017). An important feature of the Sulmona succession
89 is the presence of numerous volcanic ash (tephra) layers interbedded within the lacustrine sediment (e.g.
90 Giaccio et al., 2012, 2009). $^{40}Ar/^{39}Ar$ dating performed directly on those tephra layers provides robust
91 and independent chronological constraints for the observed variability. Giaccio et al. (2015) presented
92 the entire MIS 20 to MIS 17 interval from Sulmona, providing a relatively low-resolution stable isotope
93 record for the 820-720 ka period and with a particular focus on the length of the MIS 19c interglacial.
94 Here, this interglacial is investigated at higher resolution (sub-centennial) using a multi-proxy approach,

95 and the record is anchored to an improved chronology. We explore the environmental expression, the
96 pacing and the periodicities of the centennial- to millennial-scale variability revealed by the Sulmona
97 record. We then compare this to marine records from the mid- and high-latitudes of the North Atlantic,
98 to unravel the potential forcing and the mechanisms for short-term instability within MIS 19c at the extra-
99 regional scale.

100

101 **2. Site setting and stratigraphy**

102 The Sulmona Basin (Fig. 1) is a block-faulted intermountain depression located in the central Apennine
103 Ridge (central Italy). The basin experienced discontinuous lacustrine sediment accumulation during the
104 Quaternary (Cavinato and Miccadei, 2000; Giaccio et al., 2012, 2013). Its location and the geological,
105 stratigraphic and chronological framework were described in detail in previous studies (Giaccio et al.,
106 2009, 2012, 2013; Regattieri et al. 2015, 2016, 2017; Zanchetta et al., 2017). Briefly, the Sulmona
107 sedimentary succession is divided into three main unconformity-bounded lithostratigraphic units (SUL6,
108 SUL5 and SUL4-3), composed of alluvial, fluvial and lacustrine sediments. These units were
109 chronologically constrained by magnetostratigraphy and tephrochronology (Giaccio et al., 2012, 2013,
110 2015; Sagnotti et al., 2014, 2016). This study focuses on the outcropping 35-43 m depth interval of the
111 SUL6 lacustrine unit (Fig. 1). The SUL6 unit spans the period between MIS 20 and MIS 16 (820-650
112 ka) and encompasses the Matuyama-Brunhes geomagnetic reversal (Sagnotti et al., 2014; Mark et al.,
113 2017). The SUL6 succession has been described by Giaccio et al. (2009), with important chronological
114 amendments in Giaccio et al. (2013). Sediments are composed of light-coloured lacustrine calcareous
115 marls (Freytet and Verrecchia, 2002), with up to 90% wt $CaCO_3$ and abundant diatom remains (SOM-
116 Fig. S1). The carbonate fraction is almost entirely made up of euhedral to sub-euhedral calcite crystals
117 of ~3–5 μm (SOM-Fig. S1), typical of biologically-mediated inorganic carbonate precipitation from Ca^{2+}

and HCO_3^- ions dissolved in surface water. Hereafter we refer to it as endogenic calcite (e.g. Jones and Bowser, 1978). The contribution of clastic carbonates from the catchment is negligible and thus has no effect on the stable isotope ($\delta^{18}O$ and $\delta^{13}C$) composition of calcite (Regattieri et al., 2016, 2017). Several tephra layers occur within the SUL6 unit (Fig. 1) and form the basis of its chronology.

The topographic surface of the Sulmona basin is located between 340 and 400 m a.s.l., but its hydrology is dominated by a network of karst springs fed by recharge occurring in the surrounding mountain areas (up to 2500 m a.s.l.) (Barbieri et al., 2005; Desiderio et al., 2005a, 2005b; Falcone et al., 2008). Spring waters are characterized by a pH close to 7.5, an electrical conductivity of <500 μS and a high discharge (e.g. average 7 m^3 s^{-1} for the main spring, Capo Pescara), especially during snow melt in spring (Barbieri et al., 2005) and likely accounted for most of the paleolake recharge (Regattieri et al., 2015, 2016, 2017). Owing to the intense neotectonic activity, which has reshaped the local hydrography, the hydrological regime of Sulmona paleolake cannot be defined. However, based on the modern hydrography and hydrogeochemistry of the basin, as well as the observation that sediments are almost entirely composed of massive beds of endogenic calcite containing abundant and well-preserved diatom remains, it can be argued that it was a freshwater and hydrologically open basin. The stable isotope composition of the endogenic calcite is also consistent with this interpretation (Regattieri et al., 2015, 2016, 2017).

Local precipitation averages ~700 mm/yr but increases up to 1200 mm/yr at high altitude. Rainfall is unevenly distributed, showing maxima during autumn and winter, and minima during the summer season. Winter precipitation is mostly related to north-westerly circulation. Cyclones originate over the North Atlantic and take a mid-latitude storm track, following a prevailing NW-SE direction (Reale and Lionello, 2013). Secondary cyclones, often associated with the passage of major cyclones north of the Mediterranean, form within the basin and especially in the Gulf of Genoa, the most important Mediterranean cyclogenetic centre (Lionello et al., 2006). The amount of winter precipitation reaching the Mediterranean is influenced by several large-scale atmospheric patterns, which induce changes in

storm-track activity. In particular, at multiannual and decadal scales, the amount of winter precipitation is inversely correlated with the North Atlantic Oscillation (NAO) index (e.g. Lopez-Moreno et al., 2011; Ulbrich et al., 2012; Cullen et al., 2002), because during negative NAO phases westerly storm tracks are shifted southward and allow a greater penetration of storms into the basin, and because negative NAO phases enhance Mediterranean cyclogenesis (Ulbrich et al., 2012). Summer droughts are due to the expansion of the Azores high (Xoplaki et al., 2003; Ulbrich et al., 2012 and references therein). Summer precipitation is scarce and mostly related to local heat lows, which owe their genesis to thermal heating overland, and to evaporation and convection influenced by the surrounding mountain topography.

3. Methods

3.1. Sampling and stable isotope analyses

The studied interval comprises three distinct outcropping and partially overlapping sections that are lithostratigraphically correlated through clearly distinguishable tephra horizons (Fig. 1). The composite section is eight metres thick and was sampled for stable isotope analyses at 2.5 cm vertical resolution, for a total of ~320 samples. Sample preparation followed the procedure described in Regattieri et al. (2015). Stable isotope analyses were performed at the Stable Isotope Laboratory of the Institute of Geosciences and Earth Resources of the Italian National Research Council (IGG-CNR, Pisa, Italy) with a Gas Bench II (Thermo Scientific) coupled to a Delta XP IRMS (Finnigan), following the method presented in Regattieri et al. (2016). Sample results are reported on the VPDB scale and calibrated against the international standards NBS-18 and NBS-19. Analytical uncertainties were 0.17‰ and 0.15‰ for $\delta^{18}O$ and $\delta^{13}C$ respectively (2σ).

3.2. Elemental, mineralogical and biogenic silica analyses

X-ray fluorescence spectrometry (XRF) and X-ray powder diffraction (XRPD) analyses were performed on untreated leftover powders of the stable isotope analyses at the Earth Sciences Department of the

University of Pisa (Italy). Elemental analyses were conducted with a NITON XL3t GOLDD + hand-held XRF unit (HHXRF, see Gemelli et al., 2015 for performance), following the analytical procedure for sediment samples described in Regattieri et al. (2016).

Mineralogical composition was investigated on 36 unevenly spaced samples through XRPD analyses with a Bruker D2 Phaser diffractometer equipped with a Lynxeye fast detector. Phase identification was obtained with the Bruker Diffrac-Suite EVA and Topas-Academic software (Coelho, 2018). A semi-quantitative estimation of mineral abundances (quartz/calcite ratio, qz/ct hereafter), was calculated with the abovementioned software as the ratio between spectral peak areas of quartz and calcite.

Biogenic silica (bSi) concentrations were measured on the same samples analysed with XRF, using Fourier transform infrared spectroscopy (FTIRS) at the Institute of Geological Sciences, University of Bern, Switzerland. Analyses were performed using the method described in Vogel et al. (2008) and adopting the sample preparation protocol of Vogel et al. (2016). Calibration, accuracy and precision are detailed in Meyer-Jacob et al. (2014).

3.3. Ar/Ar dating and age modelling

The Bayesian age model (Fig. 2) is based on $^{40}Ar/^{39}Ar$ dating of six tephra layers (Fig. 1 and Table 1). Four of these tephra layers occur within the interval analysed in this study (35-43 m depth, Fig. 1), while the remaining two occur in close proximity (at 46.14 m and 29.70 m) and were employed to better constrain the age-modelling procedure. For five of the six tephra, ages are from Giaccio et al. (2015), here recalculated using the new Optimisation Model age for the ACs monitor standard (1.891 Ma; Niespolo et al., 2017). A new $^{40}Ar/^{39}Ar$ dating for the SUL2-19 tephra, obtained at the CNRS-LSCE (Centre National de la Recherche Scientifique, Laboratoire des Sciences du Climat et de l'Environnement, Gif Sur Yvette, France), is presented here (Fig. 2). Analytical procedures are as described in Giaccio et al. (2015). Details concerning the analytical procedure and the full dataset are both given in supplementary material (SOM text 1 and SOM Table 1). This new age is calibrated against

189 the ACs-2 age of 1.1891 (i.e. FCs at 28.294 Ma; Niespolo et al., 2017) and calculated using the total K
190 decay constant of Renne et al. (2010). The Bayesian age model (Fig. 2) was constructed using the Bacon
191 software (Blaauw et al., 2011). "*A priori*" settings were chosen to accommodate the actual mean
192 sedimentation rate (28.7 yr/cm), and to allow for larger variations around the mean value. Successive
193 calculations with different settings held statistically indistinguishable age-depth relationships, although
194 the current model minimizes the difference between radiometric and modelled tephra ages (Table 1).

195 *3.4. Wavelet analyses*

196 Continuous wavelet analyses (CWT) was performed on $\delta^{18}O$ data series for the whole interval between
197 800 ka and 750 ka, including lower resolution data from Giaccio et al. (2015) for the periods not covered
198 by the new record, employing a self-implemented Matlab code described in Tognarelli et al. (2018) and
199 in Tognarelli (2018). No filtering was performed before the wavelet analysis in order to preserve the
200 original frequency content of the input data. Only a linear interpolation is applied to the data to produce
201 a regular sampling over time, and a Δt of 1 yr is used as sample rate. 95% significance levels in the
202 wavelet power spectrum were computed by means of a chi-square test with two degrees of freedom,
203 where the null hypothesis assumes the that the local wavelet power spectrum corresponds to the red-
204 noise spectrum with a lag-1 coefficient of 0.73. Power bands for the most intense periodicities were
205 extracted from the spectra through the inverse continuous wavelet transform.

206 **4. Results and discussion**

207 *4.1. Chronology*

208 Full analytical details for the 35 individual sanidine crystals of the SUL2-19 tephra are given in Table
209 S1. Among the 35 analysed, 29 yielded ages overlapping within uncertainty, allowing the calculation of
210 a weighted mean age of 784.7 ± 2.4 ka (2σ including J uncertainty) (Fig. 2 and Table 1).

211 According to the age model presented in Fig. 2, the new high-resolution $\delta^{18}O$ record presented in this
212 study spans the 769.8 ± 2.2 ka to 789.9 ± 2.1 ka period. The mean associated uncertainty of the record is
213 2.6 kyr, ranging from 2.1 to 2.8 kyr (Fig. 2). The resulting average temporal resolution of the stable
214 isotope series is 60 years, while the temporal resolution of XRF and bSi analyses is 230 years. XRD
215 samples are not evenly spaced, but on average their resolution is ~ 600 years. The sedimentation rate is
216 on average 0.45 mm/yr, ranging from 0.18 mm/yr to 0.73 mm/yr.

217 *4.2. Proxy interpretation*

218 Different sediment properties presented in this work ($\delta^{13}C$, $\delta^{18}O$, Ca content, biogenic silica content
219 mineralogical composition, Fig. 3) have been measured and discussed previously for other lacustrine
220 intervals in Sulmona (Giaccio et al., 2015; Regattieri et al., 2015, 2016, 2017), so their paleoclimatic
221 interpretation is only briefly outlined here and the reader is referred to previous works for more detailed
222 explanation.

223 4.2.1 Oxygen and carbon stable isotopes

224 The oxygen stable isotope composition ($\delta^{18}O$) of lacustrine, biologically-induced, endogenic calcite
225 depends on temperature and oxygen isotopic composition of the lake surface water (e.g. Leng and
226 Marshall, 2004). In the Mediterranean region, the temperature effect during carbonate precipitation (ca.
227 -0.24‰/°C; Kim and O'Neil, 2007) is negligible, because it is counterbalanced by a gradient of ca.
228 +0.3‰/°C observed between mean annual $\delta^{18}O$ of meteoric precipitation and temperature (Bard et al.,
229 2002). The $\delta^{18}O$ of lake water depends on the $\delta^{18}O$ of precipitation and on the precipitation/evaporation
230 (P/E) ratio (e.g. Leng and Marshall, 2004). The $\delta^{18}O$ of Mediterranean precipitation has a strong
231 empirical relationship with the amount of rainfall (ca. -2‰/100 mm), with lower values related to
232 increased precipitation and higher values related to reduced precipitation (Bard et al., 2002). Previous

studies on lacustrine carbonates from the Sulmona Basin have shown that the influence of lake water evaporation for the final calcite $\delta^{18}O$ is negligible, likely due to the large and sustained karstic recharge, to presumable hydrologically open conditions and relatively short water residence times within the lake. Therefore, the $\delta^{18}O$ composition of endogenic calcite at Sulmona can be used as a first-order proxy for precipitation amount in the high-altitude catchment of the karst recharge system (Giaccio et al., 2015; Regattieri et al., 2015, 2016, 2017). Changes in isotopic composition driven by changes in the source area of moisture always contribute to changes in the $\delta^{18}O$ of precipitation, and thus of precipitated carbonates. However, these variations have proven to be significant especially during glacial/interglacial transitions (e.g. Marino et al., 2015), but can be considered negligible during interglacial periods such as the period discussed here (Tzedakis et al., 2018).

The stable carbon isotope composition of lacustrine endogenic calcite derives from that of the dissolved inorganic carbon (DIC) of the lake water (Whittington et al., 2015; Zanchetta et al., 2012, 2018;). The DIC of the Sulmona paleolake was likely significantly influenced by the input of the large karst springs recharging the basin, which today show higher $\delta^{13}C_{DIC}$ ($\delta^{13}C_{DIC(karst)}$) compared to smaller and more surficial springs, due to the longer rock-water interaction times (Falcone et al., 2008). Variations in $\delta^{13}C_{DIC(karst)}$ are related to rainfall and temperature fluctuations, with dry/cool periods characterized by reduced soil OM stocks and longer water residence times, leading to higher $\delta^{13}C_{DIC(karst)}$. Conversely, warmer and wetter conditions promote soil and vegetation development and a faster water flow, leading to more negative $\delta^{13}C_{DIC(karst)}$, as commonly inferred from speleothem studies (e.g. Genty et al., 2002; Regattieri et al., 2014). Within the lake, the $\delta^{13}C_{DIC(karst)}$ signal is mediated by additional processes, which involve equilibration with atmospheric CO_2, photosynthetic ^{12}C uptake, and consumption and recycling of organic matter in the water column as well as in the sediment. These processes largely depend on the lake hydrological budget and settings (e.g. Leng and Marshall, 2004). In our record, a generally weak covariance between $\delta^{13}C$ and $\delta^{18}O$ is observed, especially for the decreasing trend at the beginning of the

257 record and for a similar interval of enriched values at ca. 772 ka (Fig. 3). On the whole, $\delta^{13}C$ and $\delta^{18}O$
258 also show a weak though significant statistical correlation (r=0.37, Fig. 4), though is visually clear that
259 their relationship change during different intervals. A positive covariation of the two isotopes is usually
260 observed in hydrologically closed lakes (e.g. Talbot and Kelts, 1990). In hydrologically open lakes,
261 where calcite precipitation is mediated by primary productivity, an inverse relationship between $\delta^{13}C$ and
262 $\delta^{18}O$ is instead expected (e.g. Talbot and Kelts, 1990). The current hydrology of the Sulmona Basin and
263 the negligible effects of evaporation on the $\delta^{18}O$ signal strongly suggest hydrologically open conditions
264 for the Sulmona Lake, and relatively short water residence times within the lake. Thus, the weak
265 covariance between $\delta^{13}C$ and $\delta^{18}O$, rather than an indication of hydrological closure, likely indicates that
266 the $\delta^{13}C_{DIC(karst)}$ signal is dominant on the final $\delta^{13}C$ of calcite, and that the evolution of the $\delta^{13}C_{DIC(karst)}$
267 is modulated by climate conditions, mostly via the regulation of soil CO_2 leached to the lake (Zanchetta
268 et al., 2018). However, a divergence is apparent in the long-term trends of the two isotope time series,
269 with progressively more negative $\delta^{13}C$ values corresponding to increasing $\delta^{18}O$ (Fig. 3). This decoupling
270 could be related to the increasing influence of in-lake processes compared to that of karst recharge, which
271 may possibly decrease. Alternatively, the trend towards more negative $\delta^{13}C$ values can be explained by
272 the slow post-glacial development of soils in the catchment, supplying more ^{13}C depleted CO_2, following
273 the progression of the interglacial, as already observed for speleothem records from high-altitude
274 recharge areas (Drysdale et al., 2005, Regattieri et al., 2014, Zanchetta et al., 2007).

275 4.2.2 Productivity and detrital proxies

276 In the Sulmona lacustrine sediment, Ca occurs mostly as endogenic calcite, as demonstrated by previous
277 studies and by SEM microphotographs of the sediment (SOM, Fig. S1). Endogenic calcite precipitates
278 through algal fixation of CO_2, thus in this context Ca content is an indirect proxy for lake primary
279 productivity. Biogenic silica (bSi) in the sediment primarily derives from diatom frustules and thus also

provides information on primary productivity (Vogel et al., 2010). Rising spring and summer temperatures and nutrient availability promote primary productivity. Calcite precipitation rate depends also on HCO_3^- and Ca^{2+} concentrations in the lake water, with enhanced ion supply through soil/epikarst dissolution processes and high soil CO_2 production and leaching, both leading to higher dissolved ion content, during wetter and warmer periods (e.g. Francke et al., 2016). General agreement is observed between Ca and bSi content, but some differences are apparent (Fig. 3). At Sulmona, volcanic material from tephra deposition in the lake and mobilization of volcanoclastic deposits in the catchment was likely an important source for the Si and Fe needed for diatom growth. The single sample with high bSi content at ca. 789 ka occurs in close proximity (i.e. within 5 cm) of tephra T22. Tephra deposition following large eruptions can trigger short-term diatom blooms, which are not necessarily climate-related (Cvetkoska et al., 2015; D'Addabbo et al., 2015). It is also interesting that the main rise in bSi seems to lag the increase in Ca (Fig. 3). This difference could be potentially related to post-depositional dissolution of calcite. However, the sediment lithology does not show any evidence of anoxic, low pH conditions in the respective horizons (i.e. no laminations are present and the sediments are always massive, indicating continuing bioturbation and thus oxygenated conditions at the lake bottom), which would support such dissolution. Another possibility could be that hydrological variations controlling the supply of HCO_3^- and Ca^{2+} ions were less important for Fe and Si concentrations in water. This would imply a stronger dependence from rainfall fluctuations for the Ca content, whereas diatom growth (i.e. bSi content) would respond mostly to temperature variations, with superimposed fluctuations influenced by occasional Fe and Si inputs.

XRPD analyses of the bulk sediment reveal the predominant presence of calcite, accompanied only by a small amount of quartz. Quartz is typically present in small quantities in limestone. When carbonate rock dissolves, quartz remains in the soil together with other silicate minerals and Fe oxides and hydroxides. These can be transported to the lake by runoff, which is enhanced when the vegetation cover is reduced.

Part of the quartz can also be linked to erosion and transport processes from silicate rocks in the lake catchment, but these rocks are virtually absent in the Sulmona Basin, thus their contribution is likely to be insignificant. Quartz can also have an aeolian origin, as suggested for quartz-rich loess deposits along the Apennines (Giraudi et al., 2013) and for quartz grains in central Italy maar lake sediments (Narcisi, 2000). Sourcing and transport of aeolian particles is also enhanced when the vegetation is less developed (Boretto et al., 2017). Thus, at Sulmona the quartz/calcite ratio (Fig. 3) can be considered a simple, semi-quantitative way to express variations in soil erosion in the catchment and/or in aeolian input to the lake, with higher ratios indicating decreased erosion and/or reduced aeolian transport, likely both arising from vegetation development under wetter and warmer conditions.

4.3. Paleoenvironmental and paleohydrological evolution during MIS 19 in the Sulmona Basin.

Based on the interpretations introduced above, the new high-resolution $\delta^{18}O$ record for MIS 19c shows rapidly increasing precipitation after 788 ka (Fig. 3). This trend follows that observed in the low-resolution $\delta^{18}O$ time-series by Giaccio et al. (2015; Fig. 3) and represents the latest part of the deglaciation occurring between MIS 20 and MIS 19. The deglaciation is accompanied by rising lake primary productivity (increasing Ca and bSi) and by enhanced supply of soil CO_2 (lower $\delta^{13}C$), both indicating warmer temperature, and by a strong decrease in the clastic/aeolian input to the lake (decreasing qz/ct), likely arising from the increasing vegetation cover (Fig. 3). Peak precipitation was reached at ca.786.0 ka, but was rapidly interrupted by a prominent, ~0.8 kyr long, drier period starting at 785.6 ka (Fig. 3, Table 2). This event, denoted by the Roman number I in Figure 3 and in Table 2, is clearly expressed in all the other proxies. Precipitation increased again at 784.3 ka and remained relatively high until ca. 779.0 ka. Within this period, however, two events of reduced precipitation are apparent (II and III; Table 2, Fig. 3). Between 779 ka and 777 ka, precipitation ~~and primary productivity~~ decrease and conditions remain consistently drier ~~and colder~~ compared to the previous interval. Three

328 further events of increasing dryness ~~and reduced productivity~~ occur between 779 ka and 775 ka (IV, V,
329 VI; Table 2, Fig. 3). Aside from event I, changes of $\delta^{18}O$ values during event II to VI are of low
330 magnitude (0.2-0.4‰). However, all of them are coherently expressed by several data points (Fig. 3),
331 suggesting that they represent a real short-term, low-amplitude hydrological variability. These events (II
332 to VI) are not clearly expressed by the other proxies, likely due to their lower temporal resolution and to
333 a more subdued response of these properties during period of overall wet conditions. From 773.0 ka,
334 there is a large and abrupt decrease in precipitation, immediately followed by increased clastic input and
335 reduced primary productivity lasting until 771.2 ka (event VII in Fig. 3, Table 2). This period is followed
336 by an increase in precipitation and productivity (Fig. 3), although erosion rates in the catchment remain
337 quite high until the end of the high-resolution section at 769.8 ka.

338 *4.4. Regional significance of the Sulmona record and potential links with North Atlantic variability*

339 Few paleoclimatic records spanning MIS 19c with a temporal resolution comparable to our record exist
340 from the Mediterranean and the North Atlantic regions (Nomade et al., 2019, Ferretti et al., 2015;
341 Sánchez-Goñi et al., 2016), and none possesses an independent radiometric chronology. The coupled
342 marine-pollen record from marine core U1385 on the southern Iberian Margin (Hodell et al., 2015;
343 Sánchez-Goñi et al., 2016, Figs. 5 and 6) provides a relatively high-resolution, multi-proxy bio-
344 geochemical record for the MIS 19 (resolution of ~300 yr for pollen and alkenones and of ~160-200 yr
345 for planktonic and benthic stable isotope composition), capable of capturing both orbital and millennial-
346 scale climatic change (Sánchez-Goñi et al., 2016). The U1385 chronology relies on the
347 climatostratigraphic tuning to the global benthic stack LR04, and has a mean absolute uncertainty of ~5
348 ka (Lisieki and Raymo, 2005). The benthic $\delta^{18}O$ from U1385 shows that MIS 19 ranges from 791 ka to
349 758 ka, and that MIS 19c ends at ca. 775 ka. The pollen record from the same core shows that the onset
350 of the terrestrial interglacial (Tajo interglacial) occurs at ca. 787 ka, slightly after the onset of MIS 19c,

whereas its end is almost coincident with that of the benthic substage (Sánchez-Goñi et al., 2016). Seven events of forest contraction have been identified within MIS 19 (Sánchez-Goñi et al., 2016, Fig. 5). Of these, only those occurring after ca. 770 ka, i.e. well after the interglacial, appeared to be coupled with changes in oceanic conditions. For the other events, a warm sea/cold-dry land decoupling was observed and proposed to represent an increased latitudinal thermal contrast causing a northward shift in westerly wind trajectories. By analogy with the present positive mode of the NAO, this would have caused reduced precipitation over southern Iberia (Sánchez-Goñi et al., 2016), and by extension in the central and eastern Mediterranean region (e.g. Regattieri et al., 2019; Smith et al., 2016). Frequency analysis of the whole U1385 record shows evidence for a strong ~5-kyr periodicity (Sánchez-Goñi et al., 2016). This led to the conclusion that the variability observed in the pollen record can be attributed to precession harmonics-related changes in yearly solar radiation in the tropics, relaxing or amplifying the thermal latitudinal contrast and affecting mostly the strength of low-latitude low-pressure systems and thus atmospheric circulation (Sánchez-Goñi et al., 2016).

The comparison between the Sulmona and the U1385 records reveals a striking similarity between the lacustrine $\delta^{18}O$ and Mediterranean forest pollen percentage (Fig. 5). The intervals of forest reduction in the pollen record correspond to dry periods in the Sulmona record, where the higher resolution allows a better exploration of their internal structure and the identification of additional events (Fig. 5). Rainfall amount exerts a dominant control on the composition of southern European vegetation (e.g. Quezel et al., 2002; Gouveia et al., 2008) and the oxygen isotope composition of Mediterranean continental carbonates (lacustrine sediment and speleothem; e.g. Bard et al., 2002; Roberts et al., 2008), with forest expansion and ^{18}O-depleted precipitation associated with higher rainfall amount. This provides a basis for creating a common time scale between the Sulmona $\delta^{18}O$ and the Iberian margin pollen records, an approach already employed to transfer the radiometric chronology of a central Italy $\delta^{18}O$ speleothem record to a marine pollen record covering the Last Interglacial (Tzedakis et al., 2018). Thus, we aligned

375 (*sensu* Govin et al., 2015 and Zanchetta et al., 2016) the peaks in Mediterranean pollen taxa
376 corresponding to the Tajo interglacial and to the two subsequent forest expansions from U1385 to their
377 analogous wet interstadials from the Sulmona $\delta^{18}O$ record (Fig. 5 and SOM-Table 2). This adjustment
378 produces minor shifts (average ~1.7 kyr) in the U1385 chronology, fully within the absolute
379 chronological uncertainty, but it allows us to better constrain the age of Marine sub-Stage MIS 19c
380 (starting at 791 ka) and that of the terrestrial interglacial as defined by Sánchez-Goñi et al. (2016) in
381 southern Iberia (787.6 - 776.9 ka). According to the Sulmona chronology, the Tajo interglacial in U1385
382 lasts 10.7 ± 2.8 ka, which is close to a half a precession cycle. A similar duration (i.e. 11.5 ± 3.4 kyr
383 long) for the MIS19c interglacial was recently proposed by Nomade et al. (2019) based on the marine
384 section of Montalbano-Jonico (Southern Italy). The alignment between the U1385 pollen record and the
385 Sulmona isotope record allows us to explore whether the dry events from Sulmona can be associated with
386 changes in marine proxies (Fig. 6). It is worth noting that the resolution of stable-isotope analyses from
387 both archives is higher than that of the pollen and SST records, permitting a more detailed sea-land
388 comparison once a common time scale is defined. For the major events occurring at ca. 772 ka, 765 ka
389 and 760 ka based on the Sulmona chronology (VII, IIX and IX in Fig. 6), rainfall reductions are in phase
390 with prominent changes in oceanic conditions, i.e. decreasing benthic $\delta^{13}C$ and sea surface temperature
391 (SST), increasing planktonic $\delta^{18}O$ and $C_{37:4}$ -based freshwater index, Fig. 6). These events have been
392 correlated to intervals of sub-polar Ice Rafted Debris (IRD) deposition (Sánchez-Goñi et al., 2016). The
393 freshwater flux associated with IRD deposition is known to induce intervals of AMOC slow-down or
394 interruption (e.g. McManus et al., 1999). The resulting decrease in SST at the mid-latitudes reduced
395 evaporation and advection of air masses rich in moisture towards the Mediterranean region, leading to
396 basin-wide colder and drier intervals during glacial and transitional periods (i.e., glacial/interglacial
397 transition and glacial inception), (e.g. Drysdale et al., 2007; Fletcher et al 2013; Margari et al., 2009;
398 Regattieri et al., 2015, 2016; Sinopoli et al., 2018; Tzedakis et al., 2004). Together with reduced

399 precipitation, for the event at ca. 772 ka the other proxies from Sulmona also show marked decreasing
400 primary productivity in the lake and in the surroundings soils, coherently indicating decreasing
401 temperatures (Fig. 3).
402 For events not associated with iceberg discharges in the North Atlantic (I to VI in Fig. 6), marine proxies
403 do not show major oscillations, but rather a low-amplitude variability (Fig. 6). The event I at ca. 786 ka
404 appears to correspond to a decrease in planktonic $\delta^{18}O$ comprising several data points, followed by a
405 similar increase (Fig. 6). Further, the benthic $\delta^{13}C$ and the SST records show coincident slightly
406 decreasing values (Fig. 6), suggesting that this event may be connected to a slight weakening of AMOC
407 activity. To some extent, a similar configuration is apparent also for the event at ca. 782 ka (Fig. 6),
408 although it is not expressed by the benthic $\delta^{13}C$ record. For the other events, the relatively low resolution
409 and the low intensity variability hampers the possibility of a detailed correlation, though slightly
410 increased planktonic $\delta^{18}O$ values seem to correspond to event VI (Fig. 6).
411 To better define the relationship between Mediterranean hydrology and ocean conditions during the
412 interglacial, we compare our $\delta^{18}O$ record to the high-resolution (average 250 years) multiproxy record
413 from ODP-983 from the Gardar Drift, south of Iceland (Figs. 1 and 8, Kleiven et al., 2011). The Gardar
414 Drift is a key location to assess changes in NADW formation and related perturbations of AMOC
415 circulation (Kleiven et al., 2003, 2011). There, changes in deep hydrography are highlighted by decreases
416 in outflow speed and intensity from the Nordic Sea, recorded by changes in sediment grain size and
417 sorting (Kleiven et al., 2011; McCave and Hall, 2006) and by fluctuations in the benthic $\delta^{13}C$ record
418 (Oppo and Lehman, 1993). During warm periods, the site is bathed at depth by the vigorous outflow of
419 the Iceland-Scotland Overflow Water (ISOW), an essential component of the AMOC circulation that
420 modulates European climate (Bianchi and McCave, 2000). Warm salty surface waters are advected
421 northward, where the site of deep convection and NADW formation is located (Knorr and Lohmann,
422 2007; Schmidt et al., 2004). At site 983 interglacial circulation appears substantially more stable

compared to glacial periods, when the centre of NADW formation shifted from the present Nordic Seas position to the subpolar North Atlantic (Oppo and Lehman, 1993). However, all the warm stages of the Middle Pleistocene show the occurrence of rapid shifts in the style or intensity of deep-water convection, implying internal mechanisms that may generate AMOC instabilities also during periods of low ice-volume (Kleiven et al., 2003).

We first exported our independent chronology to the marine record. As discussed, events of IRD deposition in the North Atlantic impact AMOC circulation and, as a consequence, the Mediterranean hydrological cycle. Thus, we align the end of the IRD peaks occurring during the glacial inception to the corresponding onset of wet interstadials in our record (Fig. 7 and SOM-Table 2), and the end of the last IRD peak occurring during the glacial termination with the onset of the terrestrial interglacial (Fig. 8 and SOM-Table 2). As an independent test for alignment, we consider the correlations between U1385 and ODP-983, both reported on the Sulmona chronology (Fig. 7). The onset and demise of the major intervals of IRD deposition in the subpolar region show good chronological agreement with intervals of increased $C_{37:4}$ based fresh-water index (Fig. 7), despite the low resolution of the latter curve. Also, the stadial-interstadial pattern of the two planktonic $\delta^{18}O$ time-series is consistent. Decreasing/increasing $\delta^{18}O$ planktonic values can be linked to increasing/decreasing temperature or to decreased/increased salinity. In the ODP-983 record, IRD events are accompanied by decreasing planktonic $\delta^{18}O$ values (Fig. 7), likely due to the influence of ^{18}O-depleted meltwater releases, whereas on the Iberian margin the freshwater flux is associated with decreasing SST and related increases of planktonic $\delta^{18}O$ values (Fig. 7).

Now that a common time scale is defined, we can check in detail if intra-interglacial continental events have a counterpart in the sub-polar record (Fig. 8). As with U1385, the ODP-983 record shows only a subdued variability during the interglacial. However, the event I at ca. 786 ka is marked by a significant reduction in deep-water ventilation (lower benthic $\delta^{13}C$), and by a decrease in outflow strength (lower sortable silt percentage; Fig. 8), suggesting the occurrence of a short-term AMOC perturbation. It also

447 corresponds to a slight and steep decrease and a subsequent sudden increase in planktonic $\delta^{18}O$ (Fig. 8).
448 The other events recorded at Sulmona do not clearly correlate with variations in ODP-983 proxies due
449 to the subdued variability of the latter record. However, considering the combined age uncertainties, a
450 similar pattern between the deep outflow from the Nordic Sea (represented by the sortable silt percentage,
451 Fig. 8) and the Sulmona $\delta^{18}O$ record is apparent. Fluctuations in the sortable silt percentage are small,
452 but a similar variability observed during the Holocene in the record of nearby marine core NEAP-15K
453 (Bianchi and McCave, 2000) has been considered significant, and interpreted as reflecting subtle changes
454 in the ISOW strength.

455 *4.5. Forcing and pacing for millennial- to-centennial-scale variability during the MIS 19*

456 Our analyses point to different forcing for millennial and sub-millennial variability during MIS 19. After
457 the interglacial and following 772 ka, coherent changes in marine and continental proxies (Figs. 6 and 8)
458 indicate a rapid transfer of northern North Atlantic climate changes into the western Mediterranean
459 region. The North Atlantic record suggests that this variability arises from interactions between ice-sheet
460 dynamics (testified by the IRD-$C_{37:4}$ events) and the AMOC. Within the interglacial, event I centred at
461 ca. 786 ka also shows a coupling between continental and marine conditions (Figs. 6 and 8). This rainfall
462 reduction and forest contraction in southern Europe appears to be related to a temporary, low-intensity
463 AMOC disturbance. The marine records show lower benthic $\delta^{13}C$ at both sites, decreased SST on the
464 Iberian Margin, and reduced convection in the northern North Atlantic (Figs. 6 and 8). Concomitant
465 decreasing $\delta^{18}O$ planktonic values in the marine records can be related to increasing temperature, which
466 is in contrast with the SST record from the Iberian margin, or to decreased salinity, potentially related to
467 freshwater influx. This evidence suggests that this event could be an analogue to the Holocene 8.2 ka
468 event, i.e., the final outburst from the proglacial lake Agassiz (e.g. Alley et al., 1997; Alley and
469 Angustsdottir, 2005; Barber et al., 1999; Clarke et al., 2004). The related freshening of surface water

impacted convection in the Labrador Sea, where the western centre of NADW production is located, producing a slowdown of the AMOC, and a consequent widespread climate anomaly. The occurrence of similar events has been also postulated for interglacials other than Holocene, as for the Last Interglacial (Nicholl et al., 2012; Galaasen et al., 2014), and the MIS 11 (Koutsodendris et al. 2012). Interestingly, although the lower resolution and the chronological mismatching prevent a secure correlation, a short-lived period of climate perturbation is apparent within several MIS 19c records. Indeed, a cooling event in the early part of the interglacial has been reported from the pollen record of the Montalbano Jonico section (Southern Italy, Bertini et al., 2015; Marino et al., 2015), and from a marine core from the Osaka Bay (Japan, Maegakiuchi et al., 2016). For the other intra-interglacial events, the coupling between terrestrial and marine proxies, especially those from the Iberian Margin, is not as clear, perhaps pointing to a different forcing. Changes in north-westerly circulation and related moisture transport are likely involved, but the ultimate causes for these atmospheric oscillations remain currently largely unexplained. To explain changes in local convection observed at the ODP-983 site during interglacial intervals, it has been proposed that enhanced sea-ice formation south of Iceland might have created an unstable density stratification in the water column, causing a slow-down in the advection of southern warm waters, and an attendant cooling over the northern North Atlantic, with a downstream effect amplified by changes in the atmospheric circulation (Kleiven et al., 2011). State-of-the-art coupled models also have shown the occurrence of positive feedbacks between the atmosphere and the sea-ice, with stochastic atmospheric changes inducing AMOC weakening and larger sea-ice cover, leading to cooling in the sub-polar and to strengthening of high-pressure system at the high latitudes (Drijfhout et al., 2013; Kleppin et al., 2015). The similarity between the oxygen record from Sulmona and the record of deep-water ventilation and outflow speed from the Nordic Sea (Fig. 8) suggests that this cooling impacted atmospheric circulation patterns also in the Mediterranean by altering the intensity and trajectories of westerly winds. In particular, it would have led to a northern shift of the westerlies, reducing their penetration, and thus the

494 amount of rainfall, within the Mediterranean Basin. This would have resembled an atmospheric
495 configuration similar to the positive state of the NAO.
496
497 Further insights on the ultimate forcing for the MIS 19 millennial and sub-millennial variability can be
498 obtained from the dominant periodicities resulting from the Sulmona CWT analyses and by analysing
499 the timing and pacing of events. The real wavelet power spectrum for the oxygen time series, including
500 low-resolution data from Giaccio et al. (2015) for the younger (i.e. after 770 ka) and older portions (prior
501 to 790 ka) of the record, is shown in Fig. 9. Both the spectrum and the curves for the most energetic
502 periodicities (Fig. 9) show prominent changes throughout the investigated period and especially between
503 the transitional periods (deglaciation and glacial inception) and the interglacial portion of the record.
504 Considering only those periodicities which i) are enclosed in the region of greater than 95% confidence,
505 ii) fall above the COI and iii) are longer than the uncertainty associated to the record (median 2.5 kyr),
506 two main wavelength bands can be recognized. Starting from the longest, a ~5.0-6.0 kyr cycle (Fig. 9)
507 can be observed throughout the investigated period. Periodicities of ca. 5-6 kyr, i.e. similar to the fourth
508 precession harmonic have been observed in several MIS 19 records (Sánchez-Goñi et al., 2016; Ferretti
509 et al., 2016; Weirauch et al., 2008; Nomade et al., 2019). However, in our record the intensity of this
510 periodicity almost vanishes in the middle portion of the interglacial, especially between ca. 784 and 778
511 ka (Fig. 9). Further, the pacing of both intra- and post-interglacial events is non-stationary, ranging from
512 ca. 4 to 2 kyr (Table 2). The non-stationarity is evident whatever approach is used to define the temporal
513 relationships among different events, i.e. either when the onset, the mid-point and the end of events are
514 considered. The length of events is also rather variable (Table 2), with an average duration between 0.9
515 and 0.6 kyr within the interglacial and 2.3 kyr for the early glacial (Table 2). Although our observation
516 cannot rule out an initial forcing by precession harmonics, that can be modulated by sea-ice changes and
517 may affect the timing of the millennial scale variability by producing non-stationary cycles throughout

518 the MIS 19 (Ferretti et al., QSR, 2015), the observation that intra-interglacial events occur too often to
519 be explained by a 5-6 kyr cyclicity, suggest that a precession forcing is likely not the cause of intra-
520 interglacial events apparent in the Sulmona record.

521 Another significant periodicity of between ca. 4.2 and 3.5 kyr is also evident (Fig. 9), but its intensity is
522 also reduced during the MIS 19c, again suggesting that forcing of millennial and sub-millennial scale
523 variability changed between interglacial and transitional periods.

524

525 **6. Conclusions**

526 In this work, we have presented a multiproxy record (high resolution stable carbon and oxygen isotope,
527 low resolution elemental and mineralogical composition, and biogenic silica content) obtained from
528 endogenic lacustrine sediments of the Sulmona Basin (central Italy). The record is anchored onto a fully
529 independent time-scale based on $^{40}Ar/^{39}Ar$ dating of six tephra layers interbedded in the lacustrine
530 sediment, and covers the ca. 790-770 ka period, thus encompassing the interglacial portion of Marine
531 Isotope Stage MIS 19, or MIS 19c (~788-777 ka). Hydrological and environmental proxies coherently
532 indicate that the post-interglacial period is marked by major changes in climatic and environmental
533 conditions. Within the MIS19c interglacial, a low-intensity, though significant, centennial- to millennial-
534 scale hydrological and environmental variability is present and shows a non-stationary pacing. In
535 particular, a major event of rainfall reduction and environmental deterioration, ~ 1 kyr long, occurred at
536 ca. 786 ka according to our age model. Comparison of the Sulmona record with records from the Iberian
537 margin (Sánchez-Goñi et al., 2016) and from the sub-polar North Atlantic (Kleiven et al., 2011), both
538 reported on the radiometric Sulmona chronology through paleoclimatic alignment (*sensu* Govin et al.,
539 2015) points to different mechanisms operating in different periods. Major dry events on land occurring

after the end of the interglacial are associated with AMOC disruptions and increased iceberg discharge in the sub-polar north Atlantic. Within the interglacial (ca. 788-777 ka), the event at ca. 786 ka also appears related to a lower intensity perturbation of the oceanic circulation. Other intra-interglacial events are not so clearly associated with changes in marine proxies, though similarities with the sub-polar record suggest a link between rainfall amount is southern Europe and deep hydrography in the northern North Atlantic. We propose that changes in local convection, potentially related to feedbacks between atmosphere and sea-ice, may have created unstable density stratification conditions, which may have impacted the westerly circulation and the related moisture transport over the Mediterranean Basin. Noteworthy, for MIS 19 as a whole, a higher global ice volume was proposed based on modelled global sea level (Bintanja et al. 2005; Bintanja and van de Wal 2008). Possibly, this configuration would have caused a more pronounced "glacial" character for the MIS 19c interglacial, with larger global ice volume influencing dynamics and intensity of deep convection in the eastern North Atlantic, with downstream influences on rainfall variability over southern Europe. This suggests that also small changes in boundary conditions (and particularly of ice-volume and temperature) can strongly influence the millennial-scale climate variability during interglacial periods.

Acknowledgement

This work has been developed in the frame of the project HELPING (Hydrological Evolution of Past INterGlacial), funded by the National Geographic Society through an Early Career Grant assigned to E. R (CP-073ER-17). It was also part of project PRA_2018_41 "Georisorse e Ambiente" funded by the University of Pisa. $^{40}Ar/^{39}Ar$ dating was funded by the SYSTER program (INSU CNRS) assigned to S. N (ChronoBM project). ER, GZ, RND and PCT were also supported by an Australian Research Council Discovery Projects grant (DP160102969). PCT acknowledges funding from the UK Natural

563 Environment Research Council (grant NE/ I025115/1). GZ, BG and GM acknowledges funding from
564 MIUR-PRIN 2017 “Future” (leader GZ), The authors thank M.F. Sanchez-Goni, D. Hodell and T.
565 Rodrigues for providing data for comparison, and acknowledge C. Gini, A. Chitula Moura and N. Vivoli
566 for help with XRPD and J. Krbanjevic with FTIRS sample preparation and data acquisition. Ola
567 Kwiecien and three other anonymous reviewers are acknowledged for their useful comments which
568 substantially improved the quality of the manuscript.

569 **References**

570 Alley, R. B., Mayewski, P. A., Sowers, T., Stuiver, M., Taylor, K. C., Clark, P. U. 1997. Holocene
571 climatic instability: A prominent, widespread event 8200 yr ago. Geology, 25(6), 483-486.

572 Alley, R. B., Ágústsdóttir, A. M. 2005. The 8k event: cause and consequences of a major Holocene abrupt
573 climate change. Quaternary Science Reviews, 24(10-11), 1123-1149.

574 Barber, D. C., Dyke, A., Hillaire-Marcel, C., Jennings, A. E., Andrews, J. T., Kerwin, M. W., Gagnon,
575 J. M. 1999. Forcing of the cold event of 8,200 years ago by catastrophic drainage of Laurentide lakes.
576 Nature 400 (6742), 344.

577 Barbieri, M., Boschetti, T., Petitta, M., Tallini, M., 2005. Stable isotope (^{2}H, ^{18}O and $^{87}Sr/^{86}Sr$) and
578 hydrochemistry monitoring for ground water hydrodynamics analyses in a karst aquifer (Gran Sasso,
579 Central Italy). Applied Geochemistry 20, 2063–2081.

580 Bard, E., Delaygue, G., Rostek, F., Antonioli, F., Silenzi, S., Schrag, D., 2002. Hydrological conditions
581 in the western Mediterranean basin during the deposition of Sapropel 6 (~175 kyr). Earth and Planetary
582 Science Letters 202, 481–494.

583 Berger, A., Loutre, M. F. 1991. Insolation values for the climate of the last 10 million years. Quaternary
584 Science Reviews 10 (4), 297-317.

585 Bertini, A., Toti, F., Marino, M., Ciaranfi, N. 2015. Vegetation and climate across the Early–Middle
586 Pleistocene transition at Montalbano Jonico, southern Italy. Quaternary International 383, 74-88.

587 Bianchi, G. G., McCave, I. N. 2000. Hydrography and sedimentation under the deep western boundary
588 current on Björn and Gardar Drifts, Iceland Basin. Marine Geology 165(1-4), 137-169

589 Bintanja, R., van de Wal, R.S.W. 2008 North American ice-sheet dynamics and the onset of 100,000-
590 year glacial cycles. Nature 454, 869–872.

591 Bintanja, R., van de Wal, R.S.W., Oerlemans, J. 2005 Modelled atmospheric temperatures and global
592 sea levels over the past million years. Nature 437,125–128.

593 Blaauw, M., Christen, J. A. 2011. Flexible paleoclimate age-depth models using an autoregressive
594 gamma process. Bayesian analysis 6 (3), 457-474.

595 Boretto G., Zanchetta G., Ciulli A., Bini M., Fallick A.E., Lezzerini M., Colonense A.C., Zembo I.,
596 Regattieri E., Sarti, G. 2017. Stratigraphy, pedological features, paleontology, geochemistry and
597 chronology of the “loess-like” deposits of the Buca dei Corvi Section (central Italy). Catena, 151 225–
598 237-

599 Cavinato, G. P., Miccadei, E. 2000. Pleistocene carbonate lacustrine deposits: Sulmona basin (central
600 Apennines, Italy). In: Gierlowsky-Kordesch, E.H., Kelts, K.R. (Eds.), Lake Basins Through Space and
601 Time. Studies in Geology, American Association of Petroleum Geologists, 46, 517–526.

602 Clarke, G. K., Leverington, D. W., Teller, J. T., Dyke, A. S. 2004. Paleohydraulics of the last outburst
603 flood from glacial Lake Agassiz and the 8200 BP cold event. Quaternary Science Reviews 23(3-4), 389-
604 407.

605 Coelho, A. A. 2018. TOPAS and TOPAS-Academic: an optimization program integrating computer
606 algebra and crystallographic objects written in C++. Journal of Applied Crystallography 51(1), 210-218.

607 Columbu, A., Drysdale, R., Capron, E., Woodhead, J., De Waele, J., Sanna, L., Bajo, P. 2017. Early last
608 glacial intra-interstadial climate variability recorded in a Sardinian speleothem. Quaternary Science
609 Reviews 169, 391-397.

610 Cullen, H. M., Kaplan, A., Arkin, P. A. 2002. Impact of the North Atlantic Oscillation on Middle Eastern
611 climate and streamflow. Climatic Change, 55(3), 315-338.

612 Cvetkoska, A., Levkov, Z., Reed, J.M., Wagner, B., Panagiotopoulos, K., Leng, M.J., Lacey, J.H., 2015.
613 Quaternary climate change and Heinrich events in the southern Balkans: Lake Prespa
614 diatompalaeolimnology from the last interglacial to present. J. Paleolimnol. 53 (2), 215–231.

615 D'Addabbo, M., Sulpizio, R., Guidi, M., Capitani, G., Mantecca, P., Zanchetta, G., 2015. Ash leachates
616 from some recent eruptions of Mount Etna (Italy) and Popocatépetl (Mexico) volcanoes and their impact
617 on amphibian living freshwater organisms. Biogeosciences 12, 7087–7106.

618 Desiderio, G., Rusi, S., Tatangelo, F., 2005a. Utilizzo di tecniche isotopiche (^{18}O e ^{2}H) nello studio delle
619 acque sotterranee in aree protette dell'Appennino Abruzzese. Rivista Italiana Agrometeorologia 9 (1),
620 90–91.

621 Desiderio, G., Ferracuti, L., Rusi, S., Tatangelo, F., 2005b. Il contributo degli isotopi naturali ^{18}O e ^{2}H
622 nello studio delle idrostrutture carbonatiche abruzzesi e delle acque mineralizzate nell'area abruzzese e
623 molisana. Giornale Geologia Applicata 2, 453–458.

624 Drijfhout, S., Gleeson, E., Dijkstra, H. A., Livina, V. 2013. Spontaneous abrupt climate change due to
625 an atmospheric blocking-sea-ice-ocean feedback in an unforced climate model simulation. Proceedings
626 National Academy of Science. USA 110, 19713–19718.

627 Drysdale, R. N., Zanchetta, G., Hellstrom, J. C., Fallick, A. E., Zhao, J. X. 2005. Stalagmite evidence for
628 the onset of the Last Interglacial in southern Europe at 129±1 ka. Geophysical Research Letters 32(24).

629 Drysdale, R.N., Zanchetta, G., Hellstrom, J.C., Fallick, A.E., McDonald, J., Cartwright, I. 2007.
630 Stalagmite evidence for the precise timing of North Atlantic cold events during the early last glacial.
631 Geology 35, 77–80.

632 Elderfield, H., Ferretti, P., Greaves, M., Crowhurst, S., McCave, I. N., Hodell, D. A., Piotrowski, A. M.
633 2012. Evolution of ocean temperature and ice volume through the mid-Pleistocene climate transition.
634 Science 337 (6095), 704-709.

635 Falcone, R. A., Falgiani, A., Parisse, B., Petitta, M., Spizzico, M., Tallini, M. 2008. Chemical and
636 isotopic ($\delta^{18}O‰$, $\delta^{2}H‰$, $\delta^{13}C‰$, ^{222}Rn) multi-tracing for groundwater conceptual model of carbonate
637 aquifer (Gran Sasso INFN underground laboratory-central Italy). Journal of Hydrology 357, 368–388.

638 Ferretti, P., Crowhurst, S. J., Naafs, B. D. A., Barbante, C. 2015. The Marine Isotope Stage 19 in the
639 mid-latitude North Atlantic Ocean: astronomical signature and intra-interglacial variability. Quaternary
640 Science Reviews 108, 95-110.

641 Fletcher, W. J., Müller, U. C., Koutsodendris, A., Christanis, K., Pross, J. 2013. A centennial-scale record
642 of vegetation and climate variability from 312 to 240 ka (Marine Isotope Stages 9c–a, 8 and 7e) from
643 Tenaghi Philippon, NE Greece. Quaternary Science Reviews 78, 108-125.

644 Francke, A., Wagner, B., Just, J., Leicher, N., Gromig, R., Baumgarten, H., Vogel, H., Lacey, J.H.,
645 Sadori, L., Wonik, T., Leng, M. J., Zanchetta, G., Sulpizio, R., Giaccio, B., 2016. Sedimentological
646 processes and environmental variability at Lake Ohrid (Macedonia, Albania) between 637 ka and the
647 present. Biogeoscience, 13 (4),1179–1196.

648 Freytet, P., Verrecchia, E. P. 2002. Lacustrine and palustrine carbonate petrography: an overview.
649 Journal of Paleolimnology 27 (2), 221–237.

650 Galaasen, E. V., Ninnemann, U. S., Irvalı, N., Kleiven, H. K. F., Rosenthal, Y., Kissel, C., Hodell, D.
651 A. 2014. Rapid reductions in North Atlantic deep water during the peak of the last interglacial period.
652 Science 343(6175), 1129-1132.

653 Genty, D., Baker, A., Massault, M., Proctor, C., Gilmour, M., Pons-Branchu, E., Hamelin, B. 2001. Dead
654 carbon in stalagmites: carbonate bedrock paleodissolution vs. ageing of soil organic matter. Implications
655 for ^{13}C variations in speleothems. Geochimica et Cosmochimica Acta 65(20), 3443-3457.

656 Gemelli, M., D'Orazio, M., Folco, L. (2015). Chemical analysis of iron meteorites using a hand-held X-
657 ray fluorescence spectrometer. Geostandards and Geoanalytical Research 39(1), 55-69.

658 Giaccio, B., Messina, P., Sposato, A., Voltaggio, M., Zanchetta, G., Galadini, F., Gori, S., Santacroce,
659 R. 2009. Tephra layers from Holocene lake sediments of the Sulmona Basin, central Italy: implications
660 for volcanic activity in Peninsular Italy and tephrostratigraphy in the central Mediterranean area.
661 Quaternary Science Reviews 28 (25), 2710–2733.

662 Giaccio, B., Nomade, N., Wulf, S., Isaia, R., Sottili, G., Cavuoto, G., Galli, P., Messina, P., Sposato, A.,
663 Sulpizio, R., Zanchetta, G., 2012. The late MIS 5 Mediterranean tephra markers: a reappraisal from
664 peninsular Italy terrestrial records. Quaternary Science Reviews 56, 31–45.

665 Giaccio, B., Castorina, F., Nomade, S., Scardia, G., Voltaggio, M., Sagnotti, L., 2013. Revised
666 chronology of the Sulmona lacustrine succession, central Italy. Journal of Quaternary Science 28, 545–
667 551.

668 Giaccio, B., Regattieri, E., Zanchetta, G., Nomade, S., Renne, P. R., Sprain, C. J., Drysdale, R. N.,
669 Tzedakis, P. C., Messina, P., Scardia, G., Sposato, A., Bassinot, F. 2015. Duration and dynamics of the
670 best orbital analogue to the present interglacial. Geology 43 (7), 603–606.

671 Giraudi, C., Zanchetta, G., Sulpizio, R. 2013. A Late-Pleistocene phase of Saharian dust deposition in
672 the high Apennine mountains (Italy). Alpine and Mediterranean Quaternary 26, 110–122.

673 Gottschalk, J., Skinner, L. C., Misra, S., Waelbroeck, C., Menviel, L., Timmermann, A. 2015. Abrupt
674 changes in the southern extent of North Atlantic Deep Water during Dansgaard–Oeschger events. Nature
675 Geoscience 8(12), 950-953.

676 Gouveia, C., Trigo, R. M., DaCamara, C. C., Libonati, R., & Pereira, J. 2008. The North Atlantic
677 oscillation and European vegetation dynamics. International Journal of Climatology,28(14), 1835-1847.

678 Govin, A., Capron, E., Tzedakis, P. C., Verheyden, S., Ghaleb, B., Hillaire-Marcel, C., Blunier, T. 2015.
679 Sequence of events from the onset to the demise of the Last Interglacial: Evaluating strengths and
680 limitations of chronologies used in climatic archives. Quaternary Science Reviews 129, 1-36.

681 Head, M. J., Pillans, B., Farquhar, S. A. 2008. The Early-Middle Pleistocene transition: characterization
682 and proposed guide for the defining boundary. Episodes 31(2), 255.

683 Jones, B. F., Bowser, C. J. 1978. The mineralogy and related chemistry of lake sediments. In Lakes (pp.
684 179-235). Springer, New York, NY.

685 Kim, S.T., O'Neil, J.R., 1997. Equilibrium and nonequilibrium oxygen isotope effects in synthetic
686 carbonates. Geochimica and Cosmochimica Acta 61 (16), 3461–3475.

687 Kleiven, H. F., Jansen, E., Curry, W. B., Hodell, D. A., Venz, K. 2003. Atlantic Ocean thermohaline
688 circulation changes on orbital to suborbital timescales during the mid-Pleistocene. Paleoceanography
689 18(1).

690 Kleiven, H. K. F., Hall, I. R., McCave, I. N., Knorr, G., Jansen, E. 2011. Coupled deep-water flow and
691 climate variability in the middle Pleistocene North Atlantic. Geology 39(4), 343-346.

692 Kleppin, S., Jochum, M., Otto-Bliesner, B., Shields, C. A., Yeager, S. 2015. Stochastic atmospheric
693 forcing as a cause of Greenland climate transitions. Journal of Climatology 28, 7741–7763.

694 Knorr, G., and Lohmann, G., 2007, Rapid transitions in the Atlantic thermohaline circulation triggered
695 by global warming and meltwater during the last deglaciation: Geochemistry Geophysics Geosystems 8,
696 1-22.

697 Koutsodendris, A., Pross, J., Müller, U. C., Brauer, A., Fletcher, W. J., Kühl, N., Kitilova, E., Verhagen,
698 F.T.M., Lücke, A., Lotter, A. F. 2012. A short-term climate oscillation during the Holsteinian interglacial
699 (MIS 11c): An analogy to the 8.2 ka climatic event?. Global and Planetary Change 92, 224-235.

700 Leng, M. J., Marshall, J. D. 2004. Palaeoclimate interpretation of stable isotope data from lake sediment
701 archives. Quaternary Science Reviews 23, 811–831.

702 Lionello, P., Malanotte-Rizzoli, P., Boscolo, R. (Eds.). 2006. Mediterranean climate variability (Vol. 4).
703 Elsevier.

Lisiecki, L. E., Raymo, M. E. 2005. A Pliocene-Pleistocene stack of 57 globally distributed benthic $\delta^{18}O$ records. Paleoceanography 20(1).

López-Moreno, J. I., Vicente-Serrano, S. M., Morán-Tejeda, E., Lorenzo-Lacruz, J., Kenawy, A., Beniston, M. 2011. Effects of the North Atlantic Oscillation (NAO) on combined temperature and precipitation winter modes in the Mediterranean mountains: observed relationships and projections for the 21st century. Global and Planetary Change 77(1-2), 62-76.

Lüthi, D., Le Floch, M., Bereiter, B., Blunier, T., Barnola, J. M., Siegenthaler, U., Raynaud, D., Jouzel, J., Fischer, H., Kawamura, K., Stocker, T. F. 2008. High-resolution carbon dioxide concentration record 650,000–800,000 years before present. Nature 453(7193), 379.

Maegakiuchi, K., Hyodo, M., Kitaba, I., Hirose, K., Katoh, S., Sato, H. 2016. Brief sea-level fall event and centennial to millennial sea-level variations during Marine Isotope Stage 19 in Osaka Bay, Japan. Journal of Quaternary Science 31(7), 809-822.

Maiorano, P., Bertini, A., Capolongo, D., Eramo, G., Gallicchio, S., Girone, A., Pinto, P., Toti, F., Ventruti, G., Marino, M. 2016. Climate signatures through Marine Isotope Stage 19 in the Montalbano Jonico section (Southern Italy): A land–sea perspective. Palaeogeography, Palaeoclimatology, Palaeoecology 461, 341-361.

Mark, D. F., Renne, P. R., Dymock, R. C., Smith, V. C., Simon, J. I., Morgan, L. E., Staff, R.A., Ellis, B.S., Pearce, N. J. 2017. High-precision 40Ar/39Ar dating of Pleistocene tuffs and temporal anchoring of the Matuyama-Brunhes boundary. Quaternary Geochronology 39, 1-23.

Margari, V., Gibbard, P. L., Bryant, C. L., Tzedakis, P. C. (2009). Character of vegetational and environmental changes in southern Europe during the last glacial period; evidence from Lesvos Island, Greece. Quaternary Science Reviews, 28(13-14), 1317-1339.

726 Marino, M., Bertini, A., Ciaranfi, N., Aiello, G., Barra, D., Gallicchio, S., Girone, A., La Perna, R., Lirer,
727 F., Maiorano, P., Petrosino, Toti, F. 2015. Paleoenvironmental and climatostratigraphic insights for
728 Marine Isotope Stage 19 (Pleistocene) at the Montalbano Jonico succession, south Italy. Quaternary
729 International 383, 104-115.

730 Marino, G., Rohling, E. J., Rodríguez-Sanz, L., Grant, K. M., Heslop, D., Roberts, A. P., Stanford, J.D.,
731 Yu, J. (2015). Bipolar seesaw control on last interglacial sea level. Nature, 522(7555), 197.

732 McCave, I. N., Hall, I. R., 2006, Size sorting in marine muds: Processes, pitfalls, and prospects for
733 paleoflow-speed proxies: Geochemistry Geophysics Geosystems, v. 7,

734 McManus, J. F., Oppo, D. W., Cullen, J. L. (1999). A 0.5-million-year record of millennial-scale climate
735 variability in the North Atlantic. science, 283(5404), 971-975.

736 Meyer-Jacob, C., Vogel, H., Boxberg, F., Rosén, P., Weber, M. E., Bindler, R. 2014. Independent
737 measurement of biogenic silica in sediments by FTIR spectroscopy and PLS regression. Journal of
738 Paleolimnology, 52, 245-255.

739 Narcisi, B., 2000. Late Quaternary eolian deposition in central Italy. Quaternary Research 54 (2), 246–
740 252.

741 Nicholl, J. A., Hodell, D. A., Naafs, B. D. A., Hillaire-Marcel, C., Channell, J. E., Romero, O. E. 2012.
742 A Laurentide outburst flooding event during the last interglacial period. Nature Geoscience, 5(12), 901.

743 Niespolo, E. M., Rutte, D., Deino, A. L., Renne, P. R. 2017. Intercalibration and age of the Alder Creek
744 sanidine $^{40}Ar/^{39}Ar$ standard. Quaternary Geochronology 39, 205-213.

745 Nomade S., Bassinot, F., Marino, M., Simon, Q., Dewilde, F., Maiorano, P., Isguder, G., Blamart,D.,
746 Girone, A., Scao, V., Pereira, A., Toti, F., Bertini, A., Combourieu-Nebout, N., Peral, C., Bourlès, D.

747 L., Petrosino, P., Gallicchio S., and Ciaranfi, N. 2019. High-resolution foraminifer stable isotope record
748 of MIS 19 at Montalbano Jonico, southern Italy: a window into Mediterranean climatic variability during
749 a low-eccentricity interglacial. Quaternary Science Reviews 205, 106-125.

750 Oliveira, D., Desprat, S., Yin, Q., Naughton, F., Trigo, R., Rodrigues, T., Abrantes, F., Sánchez-Goñi,
751 M. F. 2017. Unravelling the forcings controlling the vegetation and climate of the best orbital analogues
752 for the present interglacial in SW Europe. Climate Dynamics 51, 1-20.

753 Oppo, D. W., Lehman, S. J. 1993. Mid-depth circulation of the subpolar north Atlantic during the last
754 glacial maximum: Science 259, 1148–1152

755 Pol, K., Masson-Delmotte, V., Johnsen, S., Bigler, M., Cattani, O., Durand, G., Falourd, S., Jouzel J.,
756 Minster B., Parrenin, F., Ritz, C., Steen-Larsen, H. C., Stenni, B. 2010. New MIS 19 EPICA Dome C
757 high-resolution deuterium data: hints for a problematic preservation of climate variability in the “oldest
758 ice”. Earth Planetary Science Letters 298, 95–103.

759 Quézel, P. 2002. Réflexions sur l'évolution de la flore et de la végétation au Maghreb méditerranéen
760 (Vol. 1). Paris: Ibis Press 112p.

761 Reale, M., Lionello, P. 2013. Synoptic climatology of winter intense precipitation events along the
762 Mediterranean coasts. Natural Hazards and Earth System Sciences 13(7), 1707-1722.

763 Renne, P. R., Mundil, R., Balco, G., Min, K., Ludwig, K. R. 2010. Joint determination of ^{40}K decay
764 constants and 40Ar∗/40K for the Fish Canyon sanidine standard, and improved accuracy for $^{40}Ar/^{39}Ar$
765 geochronology. Geochimica et Cosmochimica Acta 74 (18), 5349-5367.

766 Regattieri, E., Zanchetta, G., Drysdale, R. N., Isola, I., Hellstrom, J. C., Roncioni, A. 2014. A continuous
767 stable isotope record from the penultimate glacial maximum to the Last Interglacial (159–121 ka) from
768 Tana Che Urla Cave (Apuan Alps, central Italy). Quaternary Research 82(2), 450-461.

769 Regattieri, E., Giaccio, B., Zanchetta, G., Drysdale, R. N., Galli, P., Nomade, S., Peronace, E., Wulf, S.,
770 2015. Hydrological variability over the Apennines during the Early Last Glacial precession minimum,
771 as revealed by a stable isotope record from Sulmona Basin, Central Italy. Journal of Quaternary Science
772 30, 19-31

773 Regattieri, E., Giaccio, B., Galli, P., Nomade, S., Peronace, E., Messina P., Sposato, A., Boschi, C.,
774 Gemelli, M. 2016. A multi-proxy record of MIS 11-12 deglaciation and glacial MIS 12 instability from
775 the Sulmona Basin (central Italy). Quaternary Science Reviews 32, 129-145.

776 Regattieri, E., Giaccio, B., Nomade, S., Francke, A., Vogel, H., Drysdale, R. N., Perchiazzi, N., Wagner,
777 B., Gemelli, M., Mazzini, I., Boschi, C. Galli, P., Peronace, E. 2017. A Last Interglacial record of
778 environmental changes from the Sulmona Basin (central Italy). Palaeogeography, Palaeoclimatology,
779 Palaeoecology 472, 51-66.

780 Regattieri, E., Zanchetta, G., Isola, I., Bajo, P., Boschi, C., Perchiazzi, N., Drysdale, R. N., Boschi, C.,
781 Hellstrom, J. C., Francke, A., Wagner, B. 2018. A MIS 9/MIS 8 speleothem record of hydrological
782 variability from Macedonia (FYROM). Global and Planetary Change 162, 39-52.

783 Regattieri, E., Isola, I., Zanchetta, G., Tognarelli, A., Hellstrom, J.C., Drysdale R.N., Boschi, C.,
784 Milevski, I., Temovski, M. 2019 Middle Holocene climate variability from a stalagmite from Alilica
785 Cave (Southern Balkans). Alpine and Mediterranean Quaternary 32 (1) 2019, 1-16

786 Roberts, N., Jones, M. D., Benkaddur, A., Eastwood, W. J., Filippi, M. L., Frogley, M. R., Lamb, H. F.,
787 Leng, M. J., Reed, J. M., Stein, M., Stevens, L., Valero-Garces, B., Zanchetta, G., 2008. Stable isotope

788 records of Late Quaternary climate and hydrology from Mediterranean lakes: the ISOMED synthesis.
789 Quaternary Science Reviews 27, 2426-2441.

790 Sagnotti, L., Scardia, G., Giaccio, B., Liddicoat, J. C., Nomade, S., Renne, P. R., Sprain, C. J., 2014.
791 Extremely rapid directional change during Matuyama-Brunhes geomagnetic polarity reversal.
792 Geophysical Journal International 199, 1110–1124.

793 Sagnotti, L., Giaccio, B., Liddicoat, J. C., Nomade, S., Renne, P. R., Scardia, G., Sprain, C. J. 2016. How
794 fast was the Matuyama–Brunhes geomagnetic reversal? A new subcentennial record from the Sulmona
795 Basin, central Italy. Geophysical Journal International 204 (2), 798–812.

796 Sánchez-Goñi, M. F., Rodrigues, T., Hodell, D. A., Polanco-Martinez, J. M., Alonso-García, M.,
797 Hernández-Almeida, I., Desprat, S., Ferretti, P. 2016. Tropically-driven climate shifts in southwestern
798 Europe during MIS 19, a low eccentricity interglacial. Earth and Planetary Science Letters 448, 81-93.

799 Schmidt, M.W., Spero, H. J., Lea, D.W., 2004, Links between salinity variation in the Caribbean and
800 North Atlantic thermohaline circulation. Nature 428, 160–163.

801 Sinopoli, G., Masi, A., Regattieri, E., Wagner, B., Francke, A., Peyron, O., Sadori, L. 2018. Palynology
802 of the Last Interglacial Complex at Lake Ohrid: palaeoenvironmental and palaeoclimatic inferences.
803 Quaternary Science Reviews 180, 177-192.

804 Smith, A. C., Wynn, P. M., Barker, P. A., Leng, M. J., Noble, S. R., Tych, W. 2016. North Atlantic
805 forcing of moisture delivery to Europe throughout the Holocene. Scientific reports, 6, 24745.

806 Talbot, M. R., Kelts, K. 1990. Paleolimnological Signatures from Carbon and Oxygen Isotopic Ratios in
807 Carbonates, from Organic Carbon-Rich Lacustrine Sediments: Chapter 6. In Lacustrine Basin
808 Exploration: Case Studies and Modern Analogs. Eds by Katz, B.J., publisher AAPG

809 Tognarelli, A., Zanchetta, G., Regattieri, E., Isola, I., Drysdale, R. N., Bini, M., Hellstrom, J. C. 2018a.
810 Wavelet analysis of $\delta^{18}O$ and $\delta^{13}C$ time-series from a Holocene speleothem record from Corchia Cave
811 (central Italy): insights for the recurrence of dry-wet periods in the Central Mediterranean. Italian Journal
812 of Geosciences 137(1), 128-137.

813 Tognarelli, A. 2018. The Use of Continuous Wavelet Transform for Ground-Roll Attenuation. In 80th
814 EAGE Conference and Exhibition 2018.

815 Tzedakis, P. C., Raynaud, D., McManus, J. F., Berger, A., Brovkin, V., Kiefer, T. 2009. Interglacial
816 diversity. Nature Geoscience, 2(11), 751.

817 Tzedakis, P. C. 2010. The MIS 11 – MIS 1 analogy, southern European vegetation, atmospheric methane
818 and the "early anthropogenic hypothesis". Climate of the Past, 6, 131-144.

819 Tzedakis, P.C., Channell, J. E. T., Hodell, D. A., Kleiven, H. F. Skinner, L. C. 2012. Determining the
820 natural length of the current interglacial. Nature Geoscience, 5, 138-141.

821 Tzedakis, P.C., Drysdale, R.N., Margari, V., Skiner, L., Menviel, L., Rhodes, R.H., Taschetto, A.S.,
822 Hodell, D.A., Crowhurst, S.J., Hellstrom, J.C., Fallick, A.E., Grimalt, J.O., McManus, J.F., Martrat, B.,
823 Mokeddem, Z., Parrenin, F., Regattieri, E., Roe, K., Zanchetta, G. 2018 Enhanced climate instability in
824 the North Atlantic and southern Europe during the Last Interglacial. Nature Communications accepted,
825 DOI: 10.1038/s41467-018-06683-3

826 Tzedakis, P. C., Frogley, M. R., Lawson, I. T., Preece, R. C., Cacho, I. de Abreu, L. 2004. Ecological
827 thresholds and patterns of millennial-scale climate variability: The response of vegetation in Greece
828 during the last glacial period. Geology 32 109-112.

829 Ulbrich, U., Lionello, P., Belušić, D., Jacobeit, J., Knippertz, P., Kuglitsch, F. G., Ziv, B., 2012. Climate
830 of the Mediterranean: synoptic patterns, temperature, precipitation, winds, and their extremes. In: The
831 Climate of the Mediterranean Region—From the Past to the Future. Elsevier

832 Vogel, H., Rosén, P., Wagner, B., Melles, M., Persson, P. 2008. Fourier transform infrared spectroscopy,
833 a new cost-effective tool for quantitative analysis of biogeochemical properties in long sediment records.
834 Journal of Paleolimnology 40 (2), 689–702.

835 Vogel, H., Wagner, B., Zanchetta, G., Sulpizio, R., Rosén, P., 2010. A paleoclimatic record with
836 tephrochronological age control for the last glacial-interglacial cycle from Lake Ohrid, Albania and
837 Macedonia. Journal of Paleolimnology 44, 295–310.

838 Vogel, H., Meyer-Jacob, C., Thöle, L., Lippold, J. A., Jaccard, S. L. 2016. Quantification of biogenic
839 silica by means of Fourier transform infrared spectroscopy (FTIRS) in marine sediments. Limnology and
840 oceanography: methods 14(12), 828-838.

841 Yin, Q. Z., Berger, A. 2012. Individual contribution of insolation and CO_2 to the interglacial climates of
842 the past 800,000 years. Climate Dynamics 38(3-4), 709-724.

843 Yin, Q. Z., Berger, A. 2010. Insolation and CO 2 contribution to the interglacial climate before and after
844 the Mid-Brunhes Event. Nature Geoscience 3(4), 243.

845 Xoplaki, E., Gonzalez-Rouco, J. F., Luterbacher, J., Wanner, H., 2003. Mediterranean summer air
846 temperature variability and its connection to the large-scale atmospheric circulation and SSTs. Climate
847 Dynamics 20 (7–8), 723–739.

848 Weirauch, D., Billups, K., Martin, P. 2008. Evolution of millennial-scale climate variability during the
849 mid-Pleistocene. Paleoceanography, 23(3).

850 Whittington, G., Edwards, K. J., Zanchetta, G., Keen, D. H., Bunting, M. J., Fallick, A. E., Bryant, C. L.
851 2015. Lateglacial and early Holocene climates of the Atlantic margins of Europe: Stable isotope, mollusc
852 and pollen records from Orkney, Scotland. Quaternary Science Reviews 122, 112-130.

853 Zanchetta, G., Drysdale, R. N., Hellstrom, J. C., Fallick, A. E., Isola, I., Gagan, M. K., Pareschi, M. T.
854 2007. Enhanced rainfall in the Western Mediterranean during deposition of sapropel S1: stalagmite
855 evidence from Corchia cave (Central Italy). Quaternary Science Reviews 26(3-4), 279-286.

856 Zanchetta, G., van Welden, A., Baneschi, I., Drysdale, R.N., Sadori, L., Roberts, N., Giardini, G., Beck,
857 C., Pascucci, V., Sulpizio, R. 2012. Multiproxy record for the last 4500 years from Lake Shkodra
858 (Albania/Montenegro). Journal of Quaternary Sciences,27, 780–789.

859 Zanchetta G., Regattieri E., Giaccio B., Wagner B., Sulpizio R., Francke A., Vogel L.H., Sadori L., Masi
860 A., Sinopoli G., Lacey J.H., Leng M.L., Leicher N. (2015) Aligning MIS5 proxy records from Lake
861 Ohrid (FYROM) with independently dated Mediterranean archives: implications for core chronology.
862 Biogeosciences 13, 1-12

863 Zanchetta, G., Bini, M., Giaccio, B., Manganelli, G., Benocci, A., Regattieri, E., Colonese, A. C., Boschi,
864 C., Biagioni, C. 2017. Middle Pleistocene (MIS 14) environmental conditions in the central
865 Mediterranean derived from terrestrial molluscs and carbonate stable isotopes from Sulmona Basin
866 (Italy). Palaeogeography, Palaeoclimatology, Palaeoecology 485, 236-246.

867 Zanchetta, G., Baneschi, I., Francke, A., Boschi, C., Regattieri, E., Wagner, B., Lacey, J.H., Leng, M.,
868 Vogel, H., Sadori, L. 2018. Evidence for carbon cycling in a large freshwater lake in the Balkans over
869 the last 0.5 million years using the isotopic composition of bulk organic matter. Quaternary Science
870 Review, 202, 154-165.

871

872

873

874 **Tables and Figure Captions**

875 Table 1- Names, ages, uncertainties and depths of tephra layers used in the age-depth modelling
876 procedure. Grey cells indicate tephra occurring within the interval discussed here. *Age from Giaccio
877 et al. (2015); ** age from this study.

878 Table 2- - Age, length and pacing for events of reduced precipitation as from the Sulmona record. Roman
879 numbers are as in Figs. 3, 7 and 9; events reported in italics are from the low-resolution series from
880 Giaccio et al. (2015).

881 Figure 1- a) Location of the Sulmona Basin and of other sites mentioned in the text; b) Schematic
882 stratigraphy of the composite SUL6 lacustrine unit; c) Simplified morpho-stratigraphic scheme of the
883 Sulmona sedimentary succession.

884 Figure 2- Left panel: tephra position and labelling (see Table 1) and Bacon age model for the discussed
885 interval. The red line represents the proposed age-depth relationship, light-green lines represent 95%
886 confidence intervals. The interval highlighted in yellow represents the interval analyzed in the present
887 work. Right panel: Age probability density spectrum for the SUL2-19 tephra. Blue and grey bars are the
888 individual ages (2σ error) included and not included in the weighted mean age calculation, respectively.
889 ACs value is from Niespolo et al., 2017.

890 Figure 3- Sulmona proxy time series presented in this work. A) and B) stable oxygen and carbon isotope
891 composition of bulk lacustrine calcite ($\delta^{18}O$ and $\delta^{13}C$ composition), on A) the lower resolution δ18O
892 series from Giaccio et al. (2015) is shown as well (light blue line); C) Calcium content (XRF

893 counting*sec); D) Biogenic silica content (% wt); E) Ratio of peak areas of quartz and calcite XRD
894 analyses. Grey shadings indicate events of reduced precipitation, roman numbers are as in Table 2.

895 Figure 4- Correlation plots of $\delta^{13}C$ and $\delta^{18}O$ composition

896 Figure 5- Tuning of the U1385 pollen record (with the published chronology by Sánchez-Goñi et al.,
897 2016) on the Sulmona $\delta^{18}O$ time series (this study). Red circles indicate points used for alignment.
898 Yellow shadings indicate the events of forest contraction identified by Sanchez-Goni et al., (2016) as
899 well as the Tajo interglacial as apparent from the same record. Grey shadings are events of reduced
900 precipitation as defined in Fig. 3 and Table 2. Dotted grey lines indicate proposed correlations between
901 Sulmona and U1385 events.

902 Figure 6- Comparison between Sulmona $\delta^{18}O$ (a, light line is the lower resolution series from Giaccio et
903 al. (2015) and the U1385 record (Sánchez-Goñi et al., 2016) on the Sulmona chronology; b) U1385
904 Mediterranean forest pollen percentage; c) U1385 planktonic $\delta^{18}O$; d) U1385 benthic $\delta^{13}C$; e) U1385
905 Alkenones Sea Surface Temperature; F) U1385 percentages of alkenone $C_{37:4}$. The top panel shows the
906 U1385 benthic $\delta^{18}O$ record and MI stages and substages division. Roman numbers indicate the events of
907 reduced precipitation from the Sulmona record (see Table 2). Grey rectangles are as from Table 2 and
908 Fig. 3 and indicates events of reduced precipitation in the Sulmona basin.

909 Figure 7- Upper panel: tuning of the IRD record from core ODP-983 (Light-blue solid plot, on the
910 original chronology by Kleiven et al., 2010) on Sulmona $\delta^{18}O$ time series (this study and Giaccio et al.,
911 2015). Red circles indicate selected alignment points. Lower panel: comparison of U1385 (green,
912 planktonic $\delta^{18}O$‰ and C37:4 based freshwater index) and ODP-983 (blue, planktonic and IRD) records,
913 both reported on the Sulmona chronology. Grey rectangles indicate the intervals of IRD deposition in the
914 North Atlantic.

915 Figure 8- Comparison between Sulmona $\delta^{18}O$ and the ODP-983 record (Kleiven et al., 2011) reported
916 on the Sulmona chronology; b) ODP-938 Sortable silt percentage; c) ODP-983 planktonic $\delta^{18}O$; d) ODP-
917 983 benthic $\delta^{13}C$; Roman numbers and grey rectangles indicate the events of reduced precipitation from
918 the Sulmona record and are as shown in Table 2 and Figure 3.

919 Figure 9- Lower panel: Sulmona oxygen isotope real wavelet spectrum. The lower black line indicates
920 the cone of influence. It delimits the spectrum in two regions, where the portion below the black line may
921 be affected by edge effects and thus shows frequencies that are not significant considering the total length
922 of the record (Tognarelli et al., 2018b). The contour delimited by the black line encloses the area with a
923 confidence greater than 95%. Upper panel: the series reconstructed considering 5-6 and 4.2-4.5 kyr
924 periodicities.

925

926 Figure S1-FESEM images of Sulmona lacustrine sediment.

927

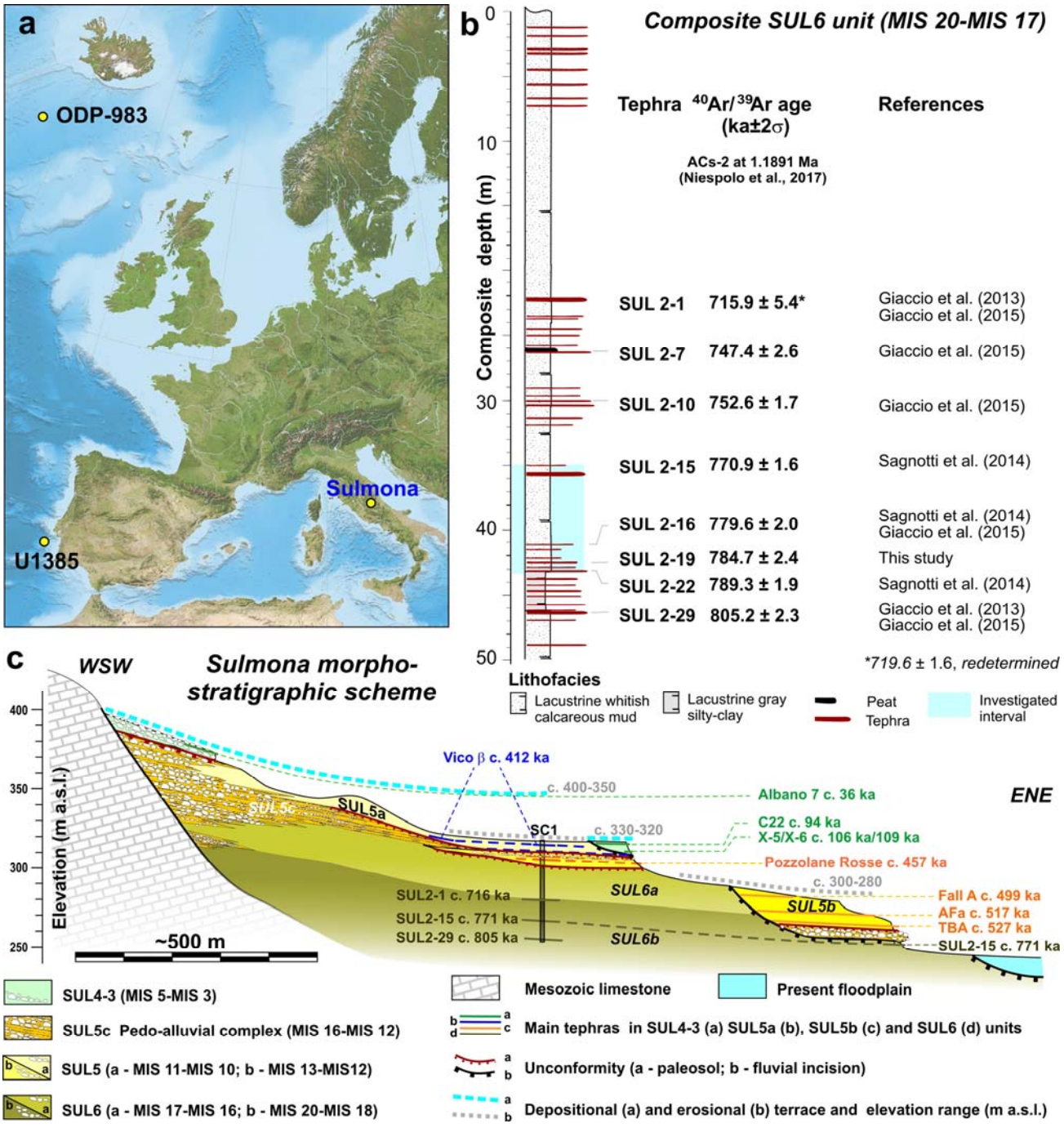

928

929 Figure 1

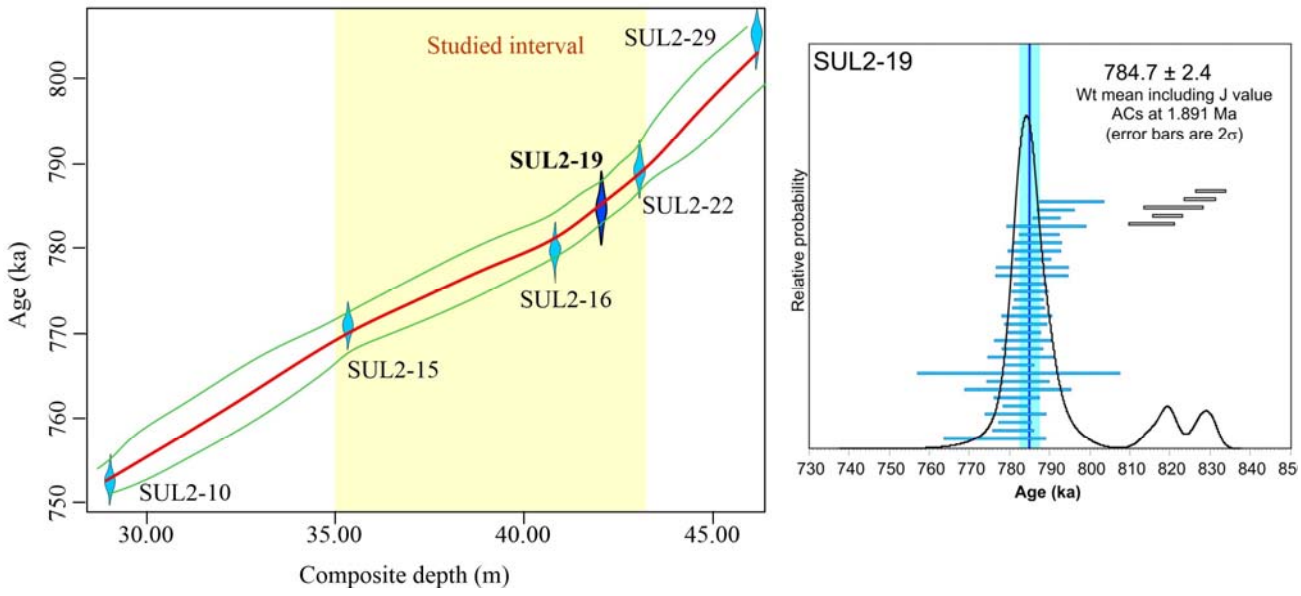

930

931 Figure 2

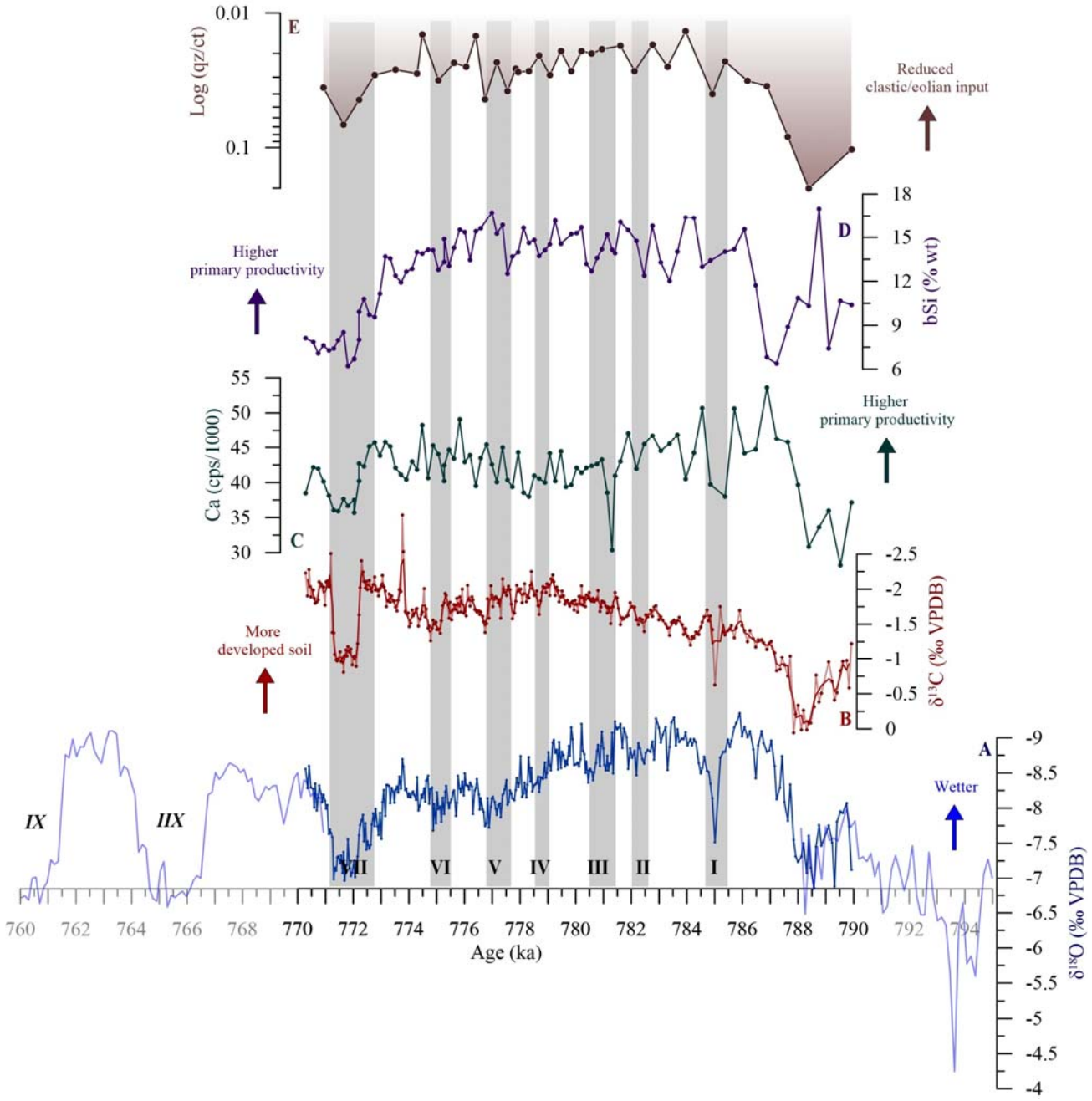
0.01
E
Log (qz/ct)
0.1
Reduced
clastic/eolian input
18
D
15
12
9
6
bSi (% wt)
Higher
primary productivity
55
50
45
40
35
30
Ca (cps/1000)
C
Higher
primary productivity
-2.5
-2
-1.5
-1
-0.5
0
δ13C (‰ VPDB)
More
developed soil
B
A
-9
-8.5
-8
-7.5
-7
-6.5
-6
-5.5
-5
-4.5
-4
δ18O (‰ VPDB)
Wetter
IX
IIX
VII
VI
V
IV
III
II
I
760
762
764
766
768
770
772
774
776
778
780
782
784
786
788
790
792
794
Age (ka)

932

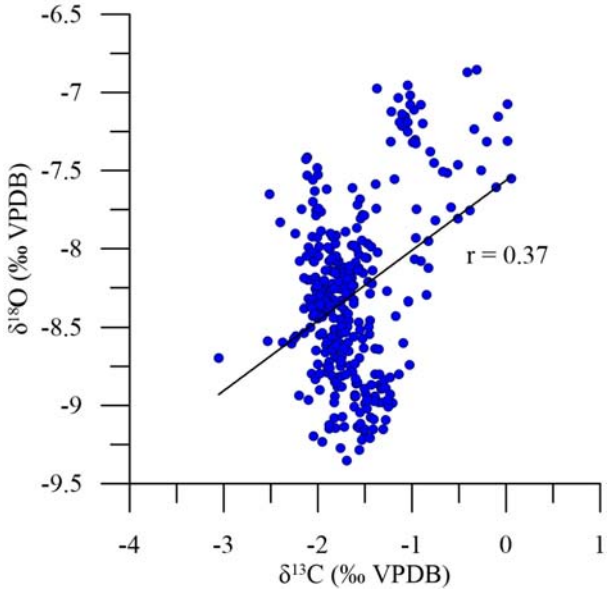

933

934 Figure 4

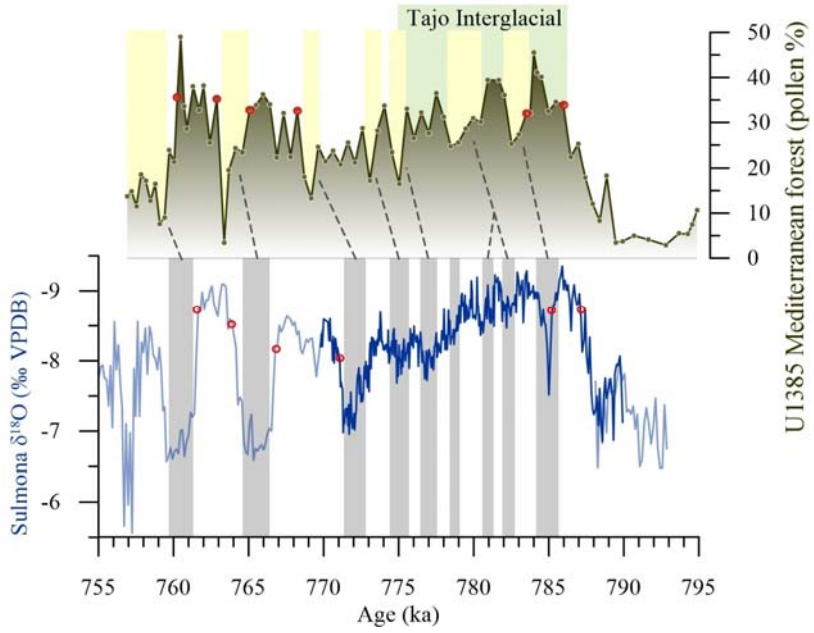

935

936 Figure 5

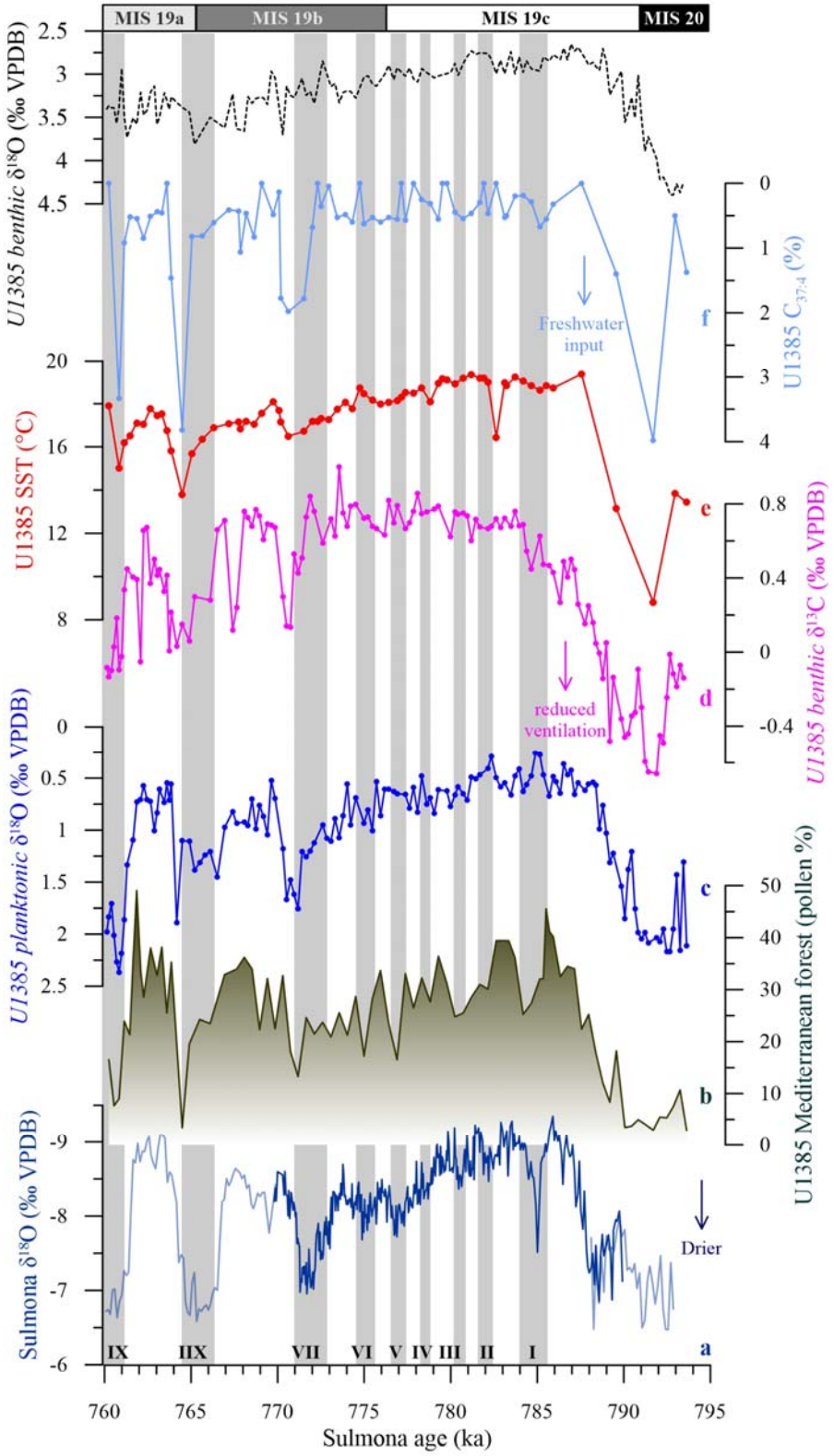
MIS 19a
MIS 19b
MIS 19c
MIS 20
U1385 benthic δ18O (‰ VPDB)
Freshwater input
f
U1385 C37:4 (%)
U1385 SST (°C)
e
U1385 benthic δ13C (‰ VPDB)
reduced ventilation
d
U1385 planktonic δ18O (‰ VPDB)
c
b
U1385 Mediterranean forest (pollen %)
Sulmona δ18O (‰ VPDB)
Drier
a
IX
IIX
VII
VI
V
IV
III
II
I
Sulmona age (ka)

937

938 Figure 6

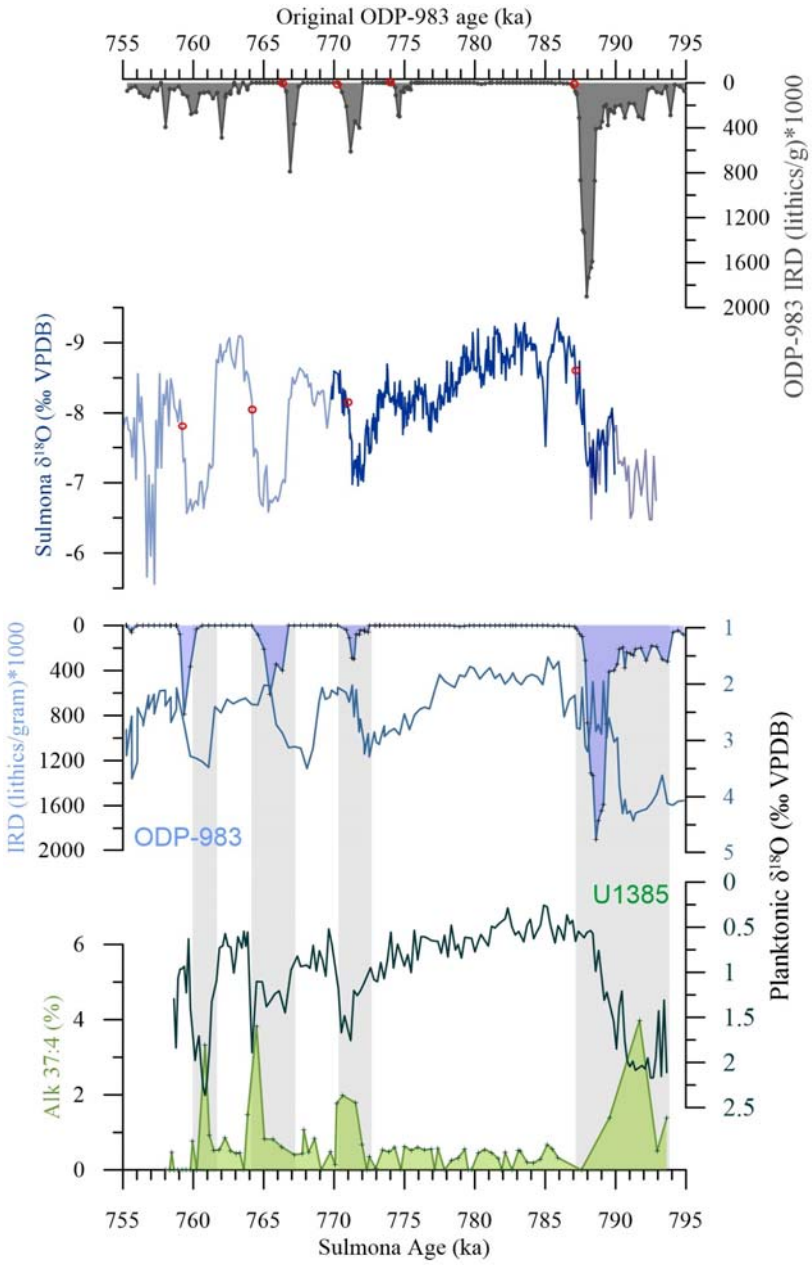

939

940 Figure 7

941

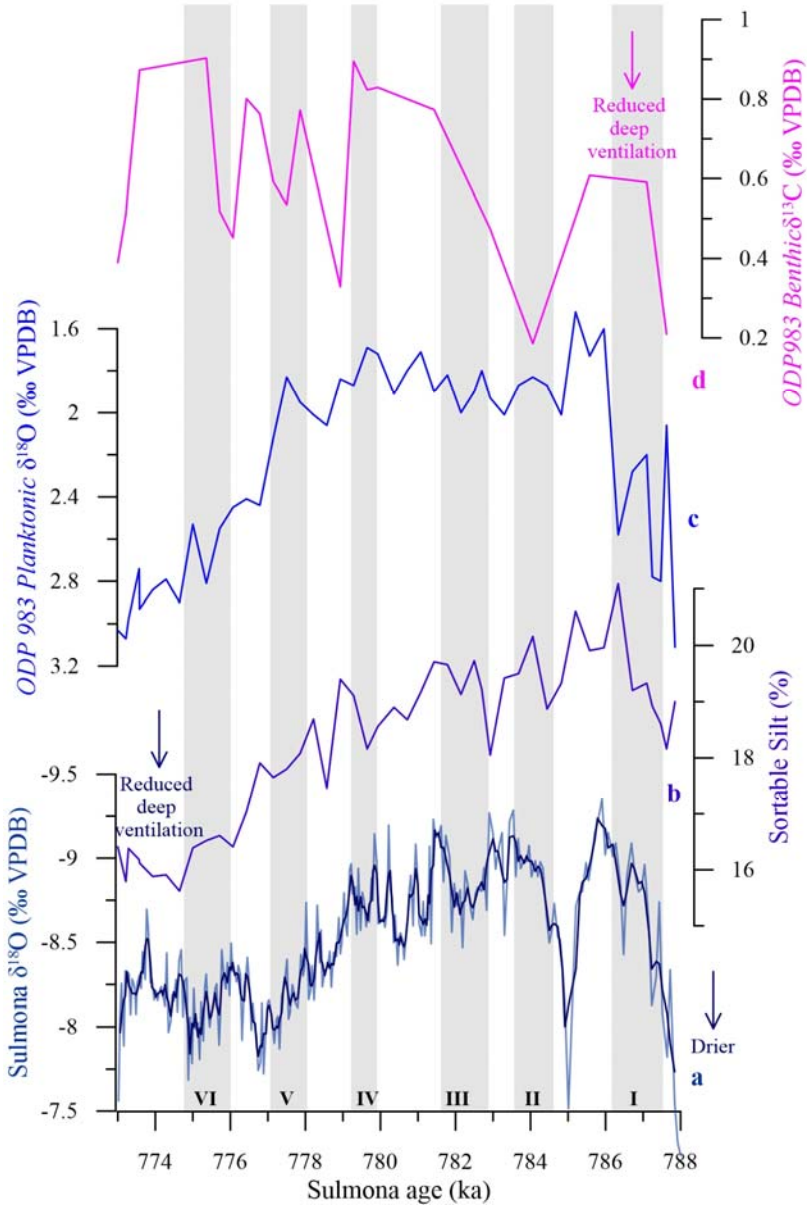

942

943 Figure 8

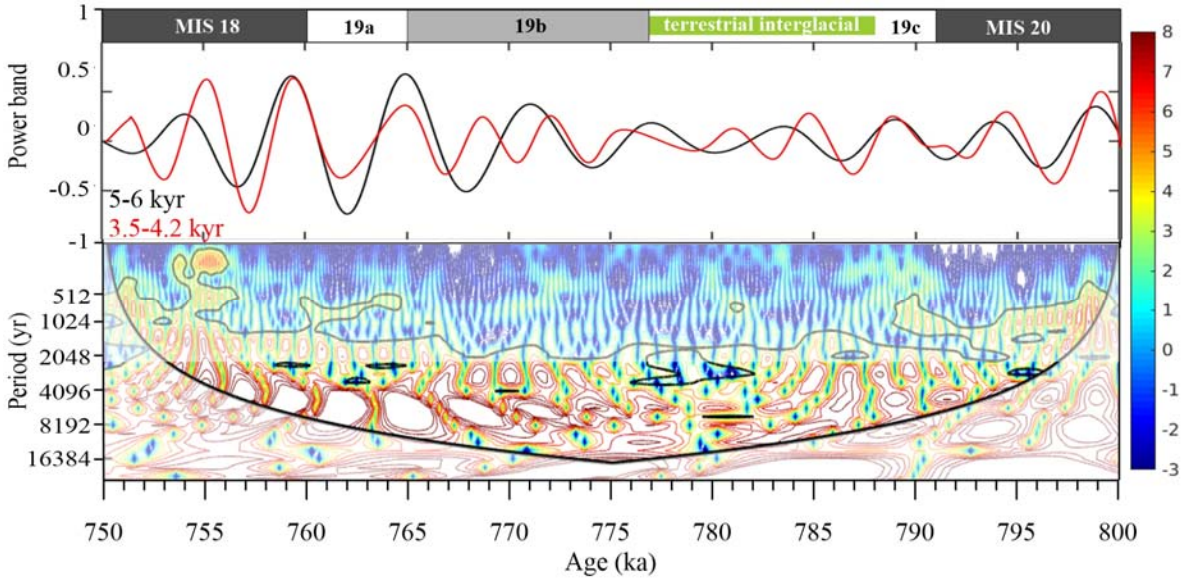

944

945 Figure 9

946